

Time-dependent approach to the X-ray photoemission problem

F. D. Picoli¹, G. Diniz¹, M. P. Lenzarini¹, I. D'Amico², L. N. Oliveira^{1*}

¹*Instituto de Física de São Carlos, Universidade de São Paulo, São Carlos, São Paulo, Brazil*

²*School of Physics, Engineering and Technology,*

University of York, York, United Kingdom

Abstract

X-ray photoemission from simple metals has been thoroughly studied, experimentally, and theoretically, in the frequency domain. Here we investigate the same problem in the time domain, with the ultimate purpose of improving the numerical renormalization-group method. We focus our study on the time dependence of the photoemission current $\mathcal{F}(t)$, a fidelity, in the terminology of quantum information. To establish benchmarks, we first calculate $\mathcal{F}(t)$ analytically and numerically for a tight-binding model. Analytically, we derive an approximate expression that becomes very precise at large times. Numerically, we diagonalize the tight-binding Hamiltonian and compute $\mathcal{F}(t)$ from its eigenvalues and eigenvectors, a straightforward procedure that covers the segment of the t axis in which the analytical expression is less accurate. The time dependence shows features of physical interest that have received little attention because they are inconspicuous in the frequency domain; the analytical expression provides a simple interpretation and traces them to an unusual form of interference. We then turn to eNRG, a recently proposed real-space variant that is more flexible than Wilson's NRG method, and present two complementary time-dependent algorithms. Comparison with the benchmarks shows that one of the eNRG algorithms yields virtually exact photocurrents with a small fraction of the computational effort to diagonalize the tight-binding Hamiltonian. The second algorithm is computationally less demanding and produces precise results at long times. In contemplation of extensions to correlated-impurity models, we identify sources of deviation and discuss the virtues and drawbacks of the two procedures.

*

I. INTRODUCTION

In this age of algorithms, methods specially designed to deal with time dependence have enriched the theory of condensed matter. Experimental progress toward understanding nonequilibrium properties [1–4], ultrafast phenomena [5–8], mesoscopic dynamics [9–11], and other enigmatic residents of the time domain has aroused interest in such methods [12–14]. The most successful numerical procedures are offshoots of time-honored techniques that have proven successful in the computation of equilibrium properties and share their virtues and limitations with the parent methods. Time-Dependent Density Functional Theory (TD-DFT) [15–19] and Time-Dependent Density Matrix Renormalization Group (TD-DMRG) [20–22] offer good illustrations. TD-DFT is remarkably successful; for example, it has extended the domain of DFT beyond the ground-state densities. Like DFT, the time-dependent version is bound by the quality of the available density functionals. Thus, while including large systems in one, two, and three dimensions, its scope is restricted to weakly correlated systems.

TD-DMRG emerged from DMRG to provide insight into the dynamical and nonequilibrium properties of strongly correlated systems [21, 23–25]. Parallel to the breadth of the parent method, the reach of TD-DMRG is limited by the dimensionality and size of the object under study [26, 27]. For the typical unidimensional Hamiltonian, this limitation is practically irrelevant, inasmuch as sufficiently long lattices fit even in small computational budgets.

Models whose properties are ruled by low-energy excitations, such as those that display Kondo physics [28–34], constitute exceptions. In this case, even the computation of equilibrium properties can be challenging. The very long lattices needed to provide the necessary energy resolution require long runs, often with prohibitive computational costs. The numerical renormalization group (NRG) method [28, 35–37], which can treat very long lattices at a small computational cost, then arises as a promising alternative. The NRG approach has been thoroughly tested in computations of ground-state, thermodynamic, excitation, and transport properties of models for correlated impurities coupled to noninteracting electrons.

Its record in the time domain is less extensive. Early attempts to compute time dependencies faced unexpected difficulties. Generalizations of Wilson’s procedure were brought forward later, with a view to overcoming such obstacles. In this context, an important advancement was achieved by Anders and Schiller [38, 39], who pointed out that excitations with large energy affect the dynamics even at long times and presented a way to overcome this complication. Costi and co-workers [40, 41] developed a special procedure to deal with pulses. More recently, two hybrid

methods have been proposed. One of them combines logarithmic and linear discretizations to study nonequilibrium transport [42, 43]. The second generalizes the NRG method by introducing thermal reservoirs to compensate for the high-energy degrees of freedom excluded from the logarithmic discretization procedure[44].

Here, moved by the desire to preserve the simplicity of the original procedure, we apply a time-dependent real-space version of Wilson’s approach to the model that supported the development of the frequency-dependent procedure. Specifically, our testbed is photoemission from a simple metal, and we examine the time dependence of the photoemission current. Physically, X radiation ejects a core electron, leaving behind a hole whose potential attracts the conduction electrons. Mathematically, the current is the *fidelity* of the quantum vector that describes the conduction electrons, that is, the modulus squared projection of the initial vector, immediately after the sudden creation of the core hole, on the vector at time t . In the laboratory, X-ray photoemission spectroscopy (XPS) measures the Fourier transform of the fidelity. X-ray absorption spectroscopy (XAS), a twin experimental technique, measures the probability of promoting a core electron to the conduction band.

Interest in XAS and XPS motivated mathematical studies in the late 1960s [45–47], which identified a power law in the near-threshold frequency dependence of each current: the Nozières-De Dominicis [46] and Doniach-Sunjic [47] laws for XAS and XPS, respectively. Subsequent research determined the prefactors of the power laws and identified a secondary threshold associated with photoemission from the bound state that the core-hole potential splits off the conduction band [48, 49]. We are unaware of parallel developments in the time domain.

The photoemission problem is more than a checkpoint in the algorithm development itinerary. The time dependence of the fidelity has features that merit physical discussion. As expected, the fidelity decreases following a Doniach-Sunjic power law, but we shall see that the decay is enveloped by a sharply defined damped oscillation. This behavior evidences interference among transitions from the initial state (the quantum state of the electron gas before absorption of the x-ray) to the final states (the excited states generated by the sudden creation of a localized potential). The occupation of the bound state sorts the final states into two classes: the *plugged* states, in which the bound state is occupied, and the *unplugged* ones, in which it is vacant. The energy needed to unplug the bound state determines the frequency of the oscillation. The damping is due to the distinct decay rates: the amplitude of the interference diminishes with time because the unplugged states decay faster than the plugged ones. In summary, the time dependence of the fidelity displays rich physics, bringing to light features that are hardly discernible in plots of the photoemission

rate as a function of frequency.

From an operational perspective, the computation of the fidelity shows outstanding advantages. In that perspective, we compare the photoemission problem with the most straightforward application of the NRG procedure, the computation of thermodynamical properties for a simple impurity model, such as the Kondo model. The latter relies on three controllable approximations. Two of them arise in the construction of the renormalization-group transformation: (i) the logarithmic discretization of the conduction band, followed by an exact Lanczos transformation, and (ii) the infrared truncation of the resulting infinite series. The renormalization-group transformation defines the iterative diagonalization procedure, whose implementation calls for an additional approximation: (iii) the ultraviolet truncation of the Hamiltonian matrix prior to its diagonalization at each iteration. As already mentioned, this straightforward truncation causes inaccuracies in computations of time-dependent properties and must be replaced by a more elaborate procedure [38]. The initial and final photoemission Hamiltonians, which are quadratic, dispense with iterative diagonalization and, consequently, with ultraviolet truncation. The computation of the fidelity thus depends on approximations (i) and (ii) only. The latter is of no concern because a minute computational effort is sufficient to control the deviations it causes. Our scrutiny will therefore be focused on the inaccuracies resulting from the discretization.

To gauge such imprecisions, we have established two benchmarks. One of them is the time dependence resulting from brute-force numerical diagonalization of the model Hamiltonian, in which the conduction band is a tight-binding Hamiltonian on a lattice with $2L$ sites. Its numerical diagonalization is straightforward for moderately large L , and this determines the fidelity up to a time proportional to L . The other benchmark is an analytical expression for the time-dependent fidelity that is very accurate, except at short times. The two benchmarks are complementary, therefore. At short and moderately large times, the numerical diagonalization yields essentially exact results. Starting at moderately large times, the analytical expression is likewise precise. From the two, we can always choose a nearly exact value for the fidelity at any time t . We call this set of data the *reference* values. Armed with them, we focus our attention on the renormalization-group procedure.

In lieu of Wilson's momentum space approach, our study is based on the equivalent real space formulation called eNRG [50]. The latter is more flexible because its construction involves three dimensionless parameters, instead of two: the *discretization* parameter, a real number $\lambda > 1$ that corresponds to Wilson's Λ ; the *sliding* parameter, a real number $1 \geq \theta \geq -1$ that corresponds to z in NRG parlance [51]; and the *offset*, a natural number ζ .

Subtraction of the reference fidelities from the output of an eNRG run with specific λ , θ , and ζ determines the absolute deviations, which fluctuate and can be relatively large. Our problem, then, is to purge the calculated fidelities from these artifacts of the discretization.

It is instructive to compare the deviations with those arising in NRG computations of thermodynamical properties. The pioneering works on the impurity magnetic susceptibility for the Kondo and Anderson models encountered irregular thermal dependencies at high temperatures and small unphysical oscillations elsewhere in plots of the susceptibility as a function of temperature. We call *transitory* the first type of deviation, and *persistent* the second. The transitory deviations are due to operators distinguishing the discretized conduction-band Hamiltonian from the corresponding fixed point of the renormalization group transformation. These operators are irrelevant: under this transformation, they decay proportionally to the energy or even faster. Their contribution to the physical properties was predicted to be significant at thermal energies of the order of the conduction bandwidth and to die out as the temperature was lowered into regions of interest on the T axis, a prediction that was confirmed by the numerical data.

The persistent deviations are mathematical analogues of the de Haas-van Alphen (dHvA) oscillations [52]. In the same way that a magnetic field gathers the continuum of conduction states into Landau levels and gives rise to the dHvA oscillations, the logarithmic discretization of the band introduces artificial oscillations in the thermal dependence of thermodynamical properties. The NRG parameter z shifts the logarithmic sequence uniformly and hence shifts the phase of the oscillatory deviations. Averaging the calculated thermodynamical property on a set of uniformly spaced z 's is therefore sufficient to remove them [51].

The same two sources of deviations arise in the calculations of the fidelity, with more damaging consequences. The irrelevant operators again give rise to transitory deviations, but their decay is slow, because it is controlled by the uncertainty principle. The discretization of the conduction levels introduces persistent fluctuations analogous to the harmonic oscillations in the thermal dependence of thermodynamical. Here, however, the persistent deviations are polychromatic, their Fourier spectrum extending to very low frequencies.

To minimize the transitory and persistent deviations, we explore two smoothing algorithms. The first is simple, conceptually, and operationally. We let the offset ζ be a large integer, fix the other eNRG parameters, and compute the fidelity from the eigenvalues and eigenvectors of the resulting Hamiltonian. This procedure yields essentially exact fidelities, free of transitory or persistent deviations, over an interval ranging from $t = 0$ to a maximum time T_ζ proportional to ζ . In other words, it solves the photoemission problem in the time domain.

As effective as this procedure to manage quadratic Hamiltonians is, the prospect of applying it to models of correlated impurities coupled to conduction bands comes with a limitation imposed by considerations of computational cost. The computational effort to diagonalize Hamiltonians of this kind grows exponentially with ζ ; it would therefore be prohibitive to adjust T_ζ to the time scale of screening in the Kondo problem, for example. However, this rapid growth does not preclude computations with smaller ζ 's, sufficient to make T_ζ encompass the decay of the transitory fluctuations. This leaves the problem of calculating the time-dependent properties for $t > T_\zeta$, which compels us to introduce the second smoothing algorithm.

The second algorithm combines averaging on ζ with numerical integration over θ [50]—an approach reminiscent of z -averaging in the NRG method [51]. Our results demonstrate that adequate tuning of the parameters eliminates the persistent fluctuations due to the discretization of the conduction energies.

Our study of the time-dependent photoemission rate therefore comprises two complementary eNRG procedures. The first offers essentially exact results over a time interval whose duration is limited by considerations of computational cost. The second is unable to deal with the transitory fluctuations, but becomes effective at long times because it effaces the persistent artifacts of the discretization. A combination of the two methods emerges as a promising tool.

The paper comprises five sections. Section II starts with the model. Section III describes the two general methods for computing the fidelity and compares illustrative numerical data with the analytical expression for the fidelity as a function of time. The physical interpretation of these reference results closes this section. Section IV presents the eNRG approach, including the large ζ procedure and integration over θ , and discusses the deviations from the reference curves as functions of the eNRG parameters. Finally, Section V gathers our conclusions.

II. MODEL

In our description of photoemission from a simple metal, a spinless tight-binding Hamiltonian represents the conduction band. The band being half filled, it is convenient to consider a lattice with an even number $2L$ of sites. The model Hamiltonian then reads

$$\mathcal{H} = \tau \sum_{\ell=0}^{2L-1} (c_\ell^\dagger c_{\ell+1} + H. c.) + K(1 - d^\dagger d) c_0^\dagger c_0, \quad (1)$$

where the first term within parentheses on the right-hand side represents the conduction band, of width 4τ , while the second term models the electrostatic interaction, of strength K , between a core

state d and the first site $c_{\ell=0}$ in the tight-binding chain. The constant K is negative, to make the interaction attractive. Notational brevity recommends the definition $\omega_\tau \equiv \tau/\hbar$.

Initially, the core level is occupied, and the last term on the right-hand side of Eq. (1) vanishes. At $t = 0$, an x-ray photon ejects the core electron to a state outside the metal and suddenly creates the attractive core-hole potential $K < 0$. The many-body state $|\Psi_t\rangle$ initially coincides with the ground state $|\Omega_0\rangle$ of the initial Hamiltonian, that is, the Hamiltonian on the right-hand side of Eq. (1) with $K = 0$. After the sudden photoejection it evolves under the final Hamiltonian

$$\mathcal{H}_K = \tau \sum_{\ell=0}^{2L-1} (c_\ell^\dagger c_{\ell+1} + H. c.) + K c_0^\dagger c_0. \quad (2)$$

III. FIDELITY

Our primary goal is to compute the squared projection, known as *fidelity*, of $|\Psi_t\rangle$ upon $|\Psi_0\rangle$:

$$\mathcal{F}(t) \equiv \left| \langle \Psi_0 | \Psi_t \rangle \right|^2. \quad (3)$$

The fidelity is of physical interest because its Fourier transform is proportional to the frequency-dependent photoemission rate measured by XPS.

A. Short-time behavior of the fidelity

Since $|\Psi_0\rangle = |\Omega_0\rangle$, given the Hamiltonian (2), the fidelity can be computed as

$$\mathcal{F}(t) = \left| \langle \Omega_0 | \exp\left(-i \frac{\mathcal{H}_K t}{\hbar}\right) | \Omega_0 \rangle \right|^2. \quad (4)$$

At $t = 0$, Eq. (4) yields $\mathcal{F} = 1$, as the definition of $\mathcal{F}(t)$ requires. To determine $\mathcal{F}(t)$ for $t > 0$, we must deal with the time-evolution operator in the matrix element. At very small times, a Trotter-Suzuki decomposition leads to a simple accurate expression. The decomposition starts out by splitting the right-hand side of Eq. (2) into the first and second terms:

$$\mathcal{H}_K = \mathcal{H}_0 + W_K, \quad (5)$$

where

$$W_K \equiv K c_0^\dagger c_0. \quad (6)$$

With the right-hand side of Eq. (5) substituted for \mathcal{H}_K , the time-evolution operator on the right-hand side of Eq. (4) is expanded in a Maclaurin series up to third order in the exponent. Rearrangement of the resulting sum then shows that

$$\begin{aligned} \exp\left(-i\frac{\mathcal{H}_K t}{\hbar}\right) &= \frac{1}{2} \left(\exp\left(-i\frac{\mathcal{H}_0 t}{\hbar}\right) \exp\left(-i\frac{W_K t}{\hbar}\right) + \exp\left(-i\frac{W_K t}{\hbar}\right) \exp\left(-i\frac{\mathcal{H}_0 t}{\hbar}\right) \right) \\ &\quad - i\frac{4}{9\pi} \left(\frac{K}{\tau}\right)^2 (\omega_\tau t)^3. \end{aligned} \quad (7)$$

At small times, the last term on the right-hand side of Eq.(7) can be dropped, and it follows that

$$\begin{aligned} \langle \Omega_0 | \exp\left(-i\frac{\mathcal{H}_K t}{\hbar}\right) | \Omega_0 \rangle &= \frac{1}{2} \left(\langle \Omega_0 | \exp\left(-i\frac{\mathcal{H}_0 t}{\hbar}\right) \exp\left(-i\frac{W_K t}{\hbar}\right) | \Omega_0 \rangle \right. \\ &\quad \left. + \langle \Omega_0 | \exp\left(-i\frac{W_K t}{\hbar}\right) \exp\left(-i\frac{\mathcal{H}_0 t}{\hbar}\right) | \Omega_0 \rangle \right) \quad \left(\left(\frac{K}{\tau}\right)^2 (\omega_\tau t)^3 \ll 1 \right), \end{aligned} \quad (8)$$

and hence that

$$\langle \Omega_0 | \exp\left(-i\frac{\mathcal{H}_K t}{\hbar}\right) | \Omega_0 \rangle = \exp\left(-i\frac{E_0 t}{\hbar}\right) \langle \Omega_0 | \exp\left(-i\frac{W_K t}{\hbar}\right) | \Omega_0 \rangle \quad \left(\left(\frac{K}{\tau}\right)^2 (\omega_\tau t)^3 \ll 1 \right). \quad (9)$$

where E_0 is the ground-state energy of the initial Hamiltonian.

The matrix-element on the right-hand side of Eq. (9) can be easily computed. Inspection of Eq. (6) shows that W_K is a projection operator. All terms in the Maclaurin expansion of $\exp\left(-i\frac{W_K t}{\hbar}\right) - 1$ are hence proportional to $c_0^\dagger c_0$, with the result

$$\exp\left(-i\frac{W_K t}{\hbar}\right) = 1 + \left(\exp\left(-i\frac{Kt}{\hbar}\right) - 1 \right) c_0^\dagger c_0. \quad (10)$$

The c_0 orbital being half filled in the initial state, it follows that

$$\langle \Omega_0 | \exp\left(-i\frac{\mathcal{H}_K t}{\hbar}\right) | \Omega_0 \rangle = \exp\left(-i\frac{E_0 t}{\hbar}\right) \frac{1 + \exp\left(-i\frac{Kt}{\hbar}\right)}{2}, \quad (11)$$

and that

$$\mathcal{F}(t) = \cos^2\left(\frac{Kt}{2\hbar}\right) \quad \left(\left(\frac{K}{\tau}\right)^2 (\omega_\tau t)^3 \ll 1 \right). \quad (12)$$

Of special interest is the initial curvature of \mathcal{F} . Differentiation of Eq. (4) proves that curvature to be proportional to the variance σ_H of the Hamiltonian:

$$\left. \frac{d^2 \mathcal{F}}{dt^2} \right|_{t=0} = -\frac{\sigma_H^2}{\hbar^2}, \quad (13)$$

where

$$\sigma_H^2 \equiv \langle \Omega_0 | \mathcal{H}^2 | \Omega_0 \rangle - \langle \Omega_0 | \mathcal{H} | \Omega_0 \rangle^2. \quad (14)$$

From Eqs. (12) and (13), it results that

$$\sigma_H^2 = \frac{K^2}{4}, \quad (15)$$

a result that can equally well be obtained from Eq. (5).

The standard deviation σ_H is equal to the quantum speed limit ν_{QSL} [53], which therefore grows without bounds as $(K/\tau) \rightarrow \infty$. In that limit, the argument of the cosine on the right-hand side of Eq. (12) reaches $\pi/2$, at $t = t_K \equiv \pi\hbar/K$, which is sufficiently short to satisfy the condition within parentheses. For $K/\tau \rightarrow \infty$, the fidelity vanishes rapidly, in agreement with Ref. [53].

If the potential is very weak, with $K/\tau \ll 1$, Eq. (12) may yield precise fidelities for $\omega_\tau t \lesssim 1$. However, we are also interested in stronger K 's, in which case the Trotter-Suzuki expansion breaks down at short times. The numerical treatment is then the simplest alternative.

B. Calculation of the fidelity

Two procedures are available to determine the time dependence of the fidelity. One of them deals with the many-body spectrum of the final Hamiltonian and will be called the *many-body* approach. The other involves only the single-particle eigenstates and eigenvalues of the initial and final Hamiltonians, and will hence be dubbed the *single-particle* method. Whereas the many-body approach is convenient for analytical manipulations, the single-particle method defines an efficient computational algorithm.

1. Many-body procedure

The vector $|\Psi_t\rangle$ can be expressed as a linear combination of the many-body eigenstates $|r\rangle$ of the Hamiltonian (2):

$$|\Psi_t\rangle = \sum_r \alpha_r \exp\left(-i\frac{E_r t}{\hbar}\right) |r\rangle, \quad (16)$$

where E_r denotes the eigenvalue associated with $|r\rangle$, and the coefficients α_r can be computed by projecting the corresponding eigenstate $|r\rangle$ upon the initial state $|\Psi_{t=0}\rangle$; Eq. (16) then yields

$\alpha_r = \langle r | \Psi_{t=0} \rangle$, equivalent to the equality

$$\alpha_r = \langle r | \Omega_0 \rangle, \quad (17)$$

which leads to a simple expression for the fidelity:

$$\mathcal{F}(t) = \left| \sum_r |\langle r | \Omega_0 \rangle|^2 \exp\left(-i \frac{E_r t}{\hbar}\right) \right|^2. \quad (18)$$

On the right-hand side of Eq. (18) a sum is multiplied by its complex conjugate. Expansion of the product shows that

$$\mathcal{F}(t) = \sum_r |\langle r | \Omega_0 \rangle|^4 + 2 \sum_{r \neq r'} |\langle r | \Omega_0 \rangle|^2 |\langle r' | \Omega_0 \rangle|^2 \cos\left(\frac{E_r - E_{r'}}{\hbar} t\right). \quad (19)$$

At $t = 0$, the phases $E_r t / \hbar$ of the exponentials in the sum on the right-hand side of Eq. (18) vanish. The sum then reduces to the normalization of $|\Omega_0\rangle$, and the equality to $\mathcal{F}(t = 0) = 1$. As t grows, the eigenstates $|r\rangle$ satisfying $|E_r| t / \hbar \gtrsim 1$ acquire different phases, and the resulting destructive interferences reduce the fidelity. At very long times, one expects the second term on the right-hand side of Eq. (19) to approach zero, and the fidelity to approach the small constant

$$c_{\text{res}} = \sum_r |\langle r | \Omega_0 \rangle|^4. \quad (20)$$

In the continuum limit $L \rightarrow \infty$, the overlaps $\langle r | \Omega_0 \rangle$ become infinitesimal, and $c_{\text{res}} \rightarrow 0$. However, for finite lattices, the sum on the right-hand side of Eq. (20), the long-time limit of the fidelity, is nonzero. The numerical results in the following sections will confirm these expectations.

Consider now the practical aspects of computing the fidelity. The quadratic Hamiltonian \mathcal{H}_0 can be easily diagonalized, analytically or numerically, to yield $2L$ nondegenerate single-particle eigenvalues. Half of them are positive, and the other half are negative. It is practical to label these energy levels in ascending order, starting with the lowest one. In this notation, the initial Hamiltonian on its diagonal basis reads

$$\mathcal{H}_0 = \sum_{n=-L}^{L-1} \varepsilon_n a_n^\dagger a_n. \quad (21)$$

where

$$\varepsilon_n = 2\tau \sin\left(\frac{\pi}{2L} \left(n + \frac{1}{2}\right)\right) \quad (n = -L, \dots, L-1) \quad (22)$$

In this sequence, the highest negative and lowest positive eigenvalues are ε_{-1} and ε_0 , respectively. In the ground state $|\Omega_0\rangle$, the negative levels ε_n ($n = -L, \dots, -1$) are filled. The Fermi level lies at zero energy, halfway between ε_{-1} and ε_0 .

For large L , in the vicinity of the Fermi level, Eq. (22) reduces to the approximate expression

$$\varepsilon_n \approx \frac{\tau\pi}{L} \left(n + \frac{1}{2} \right) \quad (|n| \ll L), \quad (23)$$

which defines a set of equally spaced levels.

The final Hamiltonian \mathcal{H}_K is particle-hole asymmetric. Nonetheless, it is still quadratic and can be likewise diagonalized:

$$\mathcal{H}_K = \sum_{n=-L}^{L-1} \epsilon_n b_n^\dagger b_n, \quad (24)$$

where

$$\epsilon_n = 2\tau \sin\left(\frac{\pi}{2L} \left(n + \frac{1}{2} - \frac{\delta}{\pi} \right)\right) \quad (n = -L, \dots, L-1), \quad (25)$$

with a phase shift δ fixed by the scattering potential and the Fermi-level density of states $\rho = 1/(\pi\tau)$:

$$\tan \delta = -\pi\rho K = -K/\tau. \quad (26)$$

For large L , close to the Fermi level, Eq. (25) takes an approximate form analogous to Eq. (23):

$$\epsilon_n \approx \frac{\tau\pi}{L} \left(n + \frac{1}{2} - \frac{\delta}{\pi} \right) \quad (|n| \ll L), \quad (27)$$

which shows that the splitting Δ_L between successive single-particle eigenvalues near the Fermi level is the same in the initial and final Hamiltonians:

$$\Delta_L = \frac{\tau\pi}{L}. \quad (28)$$

The eigenstates of \mathcal{H}_K are linear combinations of the eigenstates of \mathcal{H}_0 . With the exception of the eigenstate b_{-L} , discussed below, the linear coefficients are well described by the expression

$$\{a_m^\dagger, b_n\} = \frac{\sin(\delta)}{\varepsilon_m - \varepsilon_n} \Delta_L \quad (m = -L, \dots, L-1; n = -(L-1), \dots, L-1). \quad (29)$$

The eigenstate b_{-L} , associated with the lowest eigenvalue ε_{-L} , is a bound state. For small $|K|$, Eq. (25), with $n = -L$, also describes its energy. However, as the potential becomes more negative

and exceeds $|K| = \tau$, the lowest level splits off the bottom of the conduction band. The following equality then describes its energy:

$$\epsilon_{-L} = K + \frac{\tau^2}{K}. \quad (30)$$

Given the eigenvalues and eigenvectors of \mathcal{H}_0 and \mathcal{H}_K , it is a simple numerical exercise to compute the right-hand side of Eq. (18), for small L . The computational cost rapidly becomes prohibitive as the lattice size grows, however, because the number of many-body eigenstates contributing to the sum is

$$N_r = \binom{2L}{L}. \quad (31)$$

In practice, therefore, an alternative numerical approach is preferable.

2. Single-particle method

For long lattices, it is more practical to rewrite the projection on the right-hand side of Eq. (3) as

$$\langle \Psi_0 | \Psi_t \rangle = \langle \emptyset | a_{-1} \dots a_{-L} a_{-L}^\dagger(t) \dots a_{-1}^\dagger(t) | \emptyset \rangle, \quad (32)$$

where $a_n^\dagger(t)$ ($n = -L, \dots, L-1$) denotes the time evolution of the initial-Hamiltonian eigenstate a_n^\dagger , driven by the final-state Hamiltonian, that is,

$$a_n^\dagger(t) = e^{-i\mathcal{H}_K t/\hbar} a_n^\dagger e^{+i\mathcal{H}_K t/\hbar}, \quad (33)$$

or after projection onto the basis of the final-Hamiltonian eigenstates b_ℓ ($\ell = -L, \dots, L-1$),

$$a_n^\dagger(t) = \sum_{\ell=-L}^{L-1} \{a_n^\dagger, b_\ell\} e^{-i\epsilon_\ell t/\hbar} b_\ell^\dagger. \quad (34)$$

Wick's theorem then turns Eq. (32) into the expression

$$\langle \Psi_0 | \Psi_t \rangle = \det \underline{\underline{M}}(t), \quad (35)$$

where $\underline{\underline{M}}(t)$ is the $L \times L$ matrix with elements

$$\underline{\underline{M}}_{m,n}(t) = \sum_{\ell=-L}^{L-1} \{a_m, b_\ell^\dagger\} e^{-i\epsilon_\ell t/\hbar} \{b_\ell, a_n^\dagger\}. \quad (36)$$

The computational cost of evaluating the determinant on the right-hand side of Eq. (35) at a single instant $t = \bar{t}$ grows in proportion to L^3 . To accurately compute the fidelity at that time,

we must work with an energy splitting (28) small compared to \hbar/\bar{t} . The condition, therefore, is $L = \alpha\tau\bar{t}/\hbar$, where α is a large dimensionless number. Thus, a full calculation of the fidelity in the time interval $0 \leq t \leq t_{\max}$ requires a computational effort proportional to t_{\max}^4 . Compared with Eq. (18), Eq. (35) is overwhelmingly more efficient.

3. Time scales

The coupling τ fixes the conduction bandwidth, controls the short-time behavior of the fidelity and, within the context of numerical calculations, makes it convenient to work with dimensionless times $\omega_\tau t$, where

$$\omega_\tau \equiv \frac{\tau}{\hbar}. \quad (37)$$

At long times, with $\omega_\tau t \gg 1$, the characteristic time T_L , defined by the equality

$$\omega_\tau T_L = 2L \quad (38)$$

sets the time scale.

Specifically, comparison with Eq. (28) shows that the smallest energy in the single-particle spectrum is inversely proportional to the characteristic time; namely,

$$\Delta_L = 2\pi\hbar/T_L. \quad (39)$$

Since the energy differences in the spectra of \mathcal{H}_0 and \mathcal{H}_K are proportional to Δ_L , the periods of the oscillations that contribute to $\mathcal{F}(t)$ are multiples of the characteristic time T_L . In other words, at $t = T_L$, the fidelity completes a cycle. It follows that $\mathcal{F}(T_L) = 1$, a finite-size effect without physical equivalence in the continuum.

At moderately long times, such that $t \ll T_L$ while $\omega_\tau t \gg 1$, energies of $\mathcal{O}(\Delta_L)$ contribute insignificantly to the many-body energy in the exponent $-iE_\tau t/\hbar$ on the right-hand side of Eq. (16) and can be neglected. In this time regime, the fidelity is therefore independent of T_L . However, this independence is progressively lost as t increases. An example with $K = -2\tau$ in Sec. IV C 2 shows deviations of 0.5% at $t = T_L/10$.

4. Numerical Results

Figure 1 shows the fidelity as a function of $\omega_\tau t$, computed from Eq. (35) for the Hamiltonian (2) with $2L = 5000$ and potential scattering $K = -2\tau$. The filled red circles depict the numerical

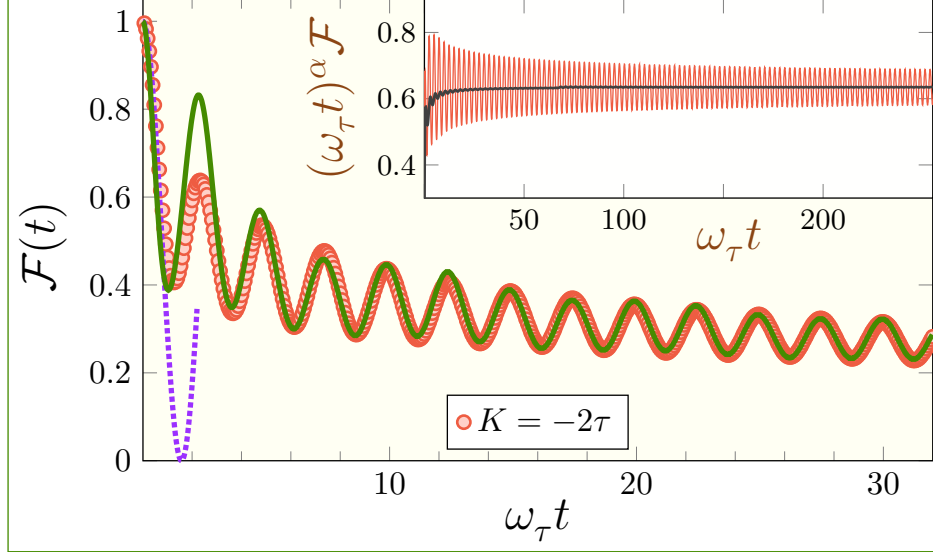


FIG. 1. Decay of the fidelity relative to the initial ground state $|\Omega_0\rangle$ following the sudden application of a localized potential $K = -2\tau$. The filled red circles represent numerical results for the tight-binding Hamiltonian (2) with $2L = 5000$ sites. The dashed purple line interrupted at $\omega_\tau t = 2$ represents Eq. (12), valid at short times only, while the solid green line depicts Eq. (56), whose accuracy grows rapidly with time. To evidence alignment with the Doniach-Sunjic power law the inset shows the numerically computed fidelity multiplied by $(\omega_\tau t)^\alpha$, where α is the Doniach-Sunjic exponent, Eq. (40). The solid black line is the running average of the ordinate over each period of oscillation.

data. For comparison, the dashed purple line displays Eq. (12), reliable at small times only. Within its validity range, for $\left(\frac{K}{\tau}\right)^2 (\omega_\tau t)^3 \ll 1$, the dashed curve fits the red circles very well. However, at $\omega_\tau t \approx 1.5$, the plots split apart, the squared cosine on the right-hand side of Eq. (12) dropping to zero and continuing to oscillate with unitary amplitude (not shown) while the circles define a damped oscillatory decay.

The inset shows that the decay of the fidelity follows the power law $F(t) \sim (\omega_\tau t)^{-\alpha}$, with the Doniach-Sunjic exponent

$$\alpha = 2 \left(\frac{\delta}{\pi}\right)^2. \quad (40)$$

The red line represents the fidelity magnified by $(\omega_\tau t)^\alpha$ as a function of $\omega_\tau t$. The black line, which represents the moving average of the ordinates over each period of oscillation, remains virtually constant after the first few cycles, showing that the long-time behavior of the fidelity conforms to the Doniach-Sunjic power law. Still, the inset leaves two questions unanswered, since it does not explain why the fidelity oscillates or why the amplitude of the oscillations decays, even after multiplication by $(\omega_\tau t)^\alpha$.

To track the origin of the damped oscillations, it is necessary to examine the eigenstates of the final-state Hamiltonian \mathcal{H}_K that contribute to the fidelity, that is, the many-body eigenstates comprising L occupied levels. The bound state b_{-L} , with energy ϵ_{-L} , is special among the single-particle eigenstates. Since its occupation $n_{-L} \equiv b_{-L}^\dagger b_{-L}$ is conserved, the many-body eigenstates $|r\rangle$ of \mathcal{H}_K can be divided into two classes, depending on whether $n_{-L} = 1$ or $n_{-L} = 0$. The depiction in Fig. 2 suggests the adjectives *plugged* and *unplugged* to label the former and the latter eigenstates, respectively. The lowest-energy plugged state is the ground state $|\Omega\rangle$ of the final Hamiltonian \mathcal{H}_K , with energy E_0 . The lowest unplugged state is $b_0^\dagger b_{-L} |\Omega\rangle$, since b_0 is the first single-particle level with positive energy, and its energy is $E_0 + \epsilon_B$, where ϵ_B is the energy needed to promote an electron from the bound state to the first unoccupied level above the Fermi level, as the double-headed arrow in the figure indicates:

$$\epsilon_B = \frac{\Delta_L}{2} - \epsilon_{-L}. \quad (41)$$

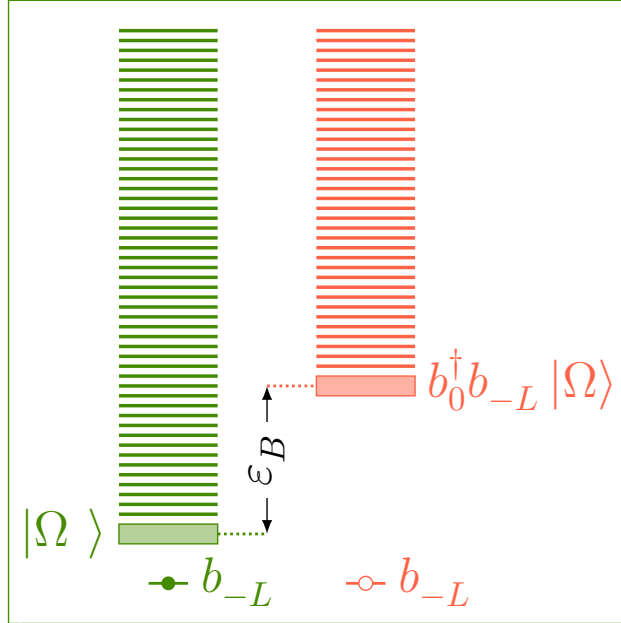


FIG. 2. Classification of the final many-body eigenstates with L electrons. The left (right) column shows the *plugged* (*unplugged*) eigenstates, in which the bound level b_{-L} is filled (vacant). The green (red) bold horizontal dash represents the ground state (lowest unplugged state), and the green (red) horizontal segments above it are many-body excited states.

Now, let \mathcal{P} denote the set of all the plugged states and \mathcal{U} , the set of the unplugged states. There is a one-to-one correspondence between the states in \mathcal{P} and in \mathcal{U} . To verify this statement, take any plugged state $|P\rangle \in \mathcal{P}$ and construct a many-body state $|U\rangle$ so that (i) the bound state be

vacant and (ii) the occupation of each level ϵ_p ($p = -L + 1, \dots, L - 1$) be equal to the occupation of level ϵ_{p-1} in $|P\rangle$.

As the arrows in Fig. 3(a) indicate, the energy difference between $|U\rangle$ and $|P\rangle$ is

$$E_U - E_P = \epsilon_{-L+1} - \epsilon_{-L} + (L - 1)\Delta_L, \quad (42)$$

and since $(L - 1)\Delta_L$ is the energy difference between ϵ_{-L+1} and ϵ_0 , it follows from Eq. (41) that

$$E_U - E_P = \epsilon_B. \quad (43)$$

One class of plugged states requires special handling. The assignment depicted by the arrows in Fig. 3(a) is inapplicable to plugged states such as $|P'\rangle$ in Fig. 3(b), in which the highest energy level ϵ_{L-1} is occupied; moreover, the assignment in panel (a) never yields unplugged states such as $|U'\rangle$, in which the level $\epsilon_{-(L-1)}$ is vacant. Nonetheless, the special construction described by the arrows in Fig. 3(b) associates $|P'\rangle$ with $|U'\rangle$ and guarantees the energy difference between the two states to satisfy the equality

$$E_{U'} - E_{P'} = \epsilon_B. \quad (44)$$

Together, the assignments in panels (a) and (b) of Fig. 3 associate a unique unplugged state with each plugged state. The assignments can be reversed to associate a unique plugged state with each unplugged state. This verifies the statement above that there is a one-to-one correspondence between the plugged and unplugged states. Moreover, the energy difference between each unplugged state and the matching plugged state is ϵ_B , as Eqs. (42) and (41) show.

This conclusion, that the energy separation between each plugged eigenstate $|P\rangle$ and the corresponding unplugged eigenstate $|U\rangle$ is uniform, recommends the partition of the sum on the right-hand side of Eq. (18), that is, that we write

$$\mathcal{F}(t) = \left| \mathcal{P}_P + \exp(-i\omega_B t) \mathcal{P}_U \right|^2. \quad (45)$$

Here, $\omega_B \equiv \epsilon_B/\hbar$,

$$\mathcal{P}_P \equiv \sum_P \left| \langle P | \Omega_0 \rangle \right|^2 \exp\left(-i \frac{E_P t}{\hbar}\right), \quad (46)$$

and

$$\mathcal{P}_U \equiv \sum_U \left| \langle U | \Omega_0 \rangle \right|^2 \exp\left(-i \frac{E_U t}{\hbar}\right), \quad (47)$$

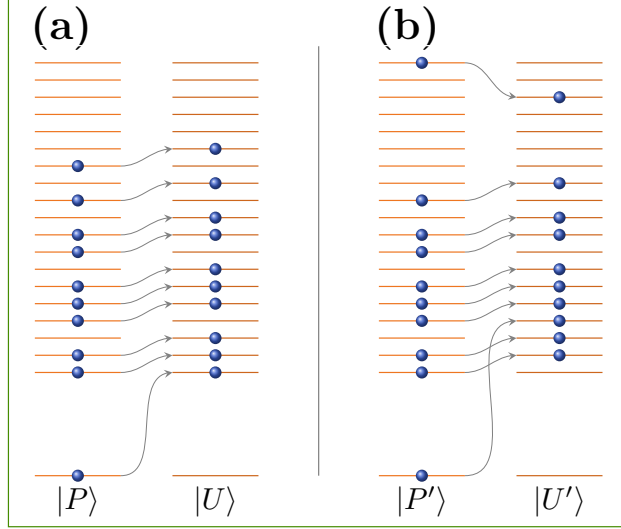


FIG. 3. Construction of unplugged many-body eigenstates from plugged eigenstates. In each panel, the orange horizontal lines depict single-particle levels, and the blue circles mark the occupied levels. The bound state, split off the bottom of the conduction band, is occupied in the plugged state and vacant in the unplugged one. Panel (a) depicts the standard construction, applicable to plugged states with vacant highest-energy conduction level. As the curved arrows indicate, for each occupied level in $|P\rangle$, the construction then fills the next higher-energy level in $|U\rangle$, as the curved arrows indicate. Panel (b) shows the special construction required when the highest-energy level in $|P\rangle$ is occupied. As the curved arrows indicate, the occupied levels in $|P'\rangle$ between the bound-state energy ϵ_{-L} and the highest energy ϵ_{L-1} follow the upgrade rule in panel (a). The electron in the bound-state level is then promoted to the first vacant level above ϵ_{-L} in $|U'\rangle$, and the electron in level ϵ_{L-1} is demoted so that the energy difference between the unplugged and plugged states satisfies Eq. (44).

where the sums span the sets of the plugged eigenstates $|P\rangle$ and the unplugged eigenstates $|U\rangle$, respectively. In Eq. (47), $E_P = E_U - \epsilon_B$ denotes the energy of the plugged eigenstate associated with $|U\rangle$.

Although the time-dependent exponentials on the right-hand sides of Eqs. (46) and (47) are identical, the projections $\langle P|\Omega_0\rangle$ and $\langle U|\Omega_0\rangle$ are different and therefore deserve special attention. Consider a filled level n in the initial ground state $|\Omega_0\rangle$ and a filled level p in the plugged state $|P\rangle$ in Fig. 3(a). Assuming that neither level lies too far from the Fermi level, so that Eqs. (22) and (25) are reliable, the initial energy ϵ_n and the final energy ϵ_p differ by

$$\epsilon_n - \epsilon_p = \Delta_L \left(n - p + \frac{\delta}{\pi} \right). \quad (48)$$

The difference on the left-hand side of Eq. (48) is the denominator of the fraction on the right-hand side of Eq. (29) and hence determines the projection $\{a_n^\dagger, b_p\}$ between the two single-particle

eigenstates. The projection $\langle P|\Omega_0\rangle$ is the determinant of the $L \times L$ matrix whose elements are the projections between the occupied single-particle states in $|P\rangle$ and $|\Omega_0\rangle$.

Next, consider the levels occupied in the unplugged state $|U\rangle$. To each level p in the many-body state $|P\rangle$, the construction in Fig. 3 associates a filled level $u = p + 1$ in $|U\rangle$. The energy difference between the initial level n and the final level u is

$$\Delta\mathcal{E}_{u,n} \equiv \varepsilon_n - \epsilon_u = \frac{\tau\pi}{L} \left(n - (p + 1) + \frac{\delta}{\pi} \right), \quad (49)$$

which can be rewritten to bring out the similarity to the right-hand side of Eq. (48):

$$\varepsilon_n - \epsilon_u = \frac{\tau\pi}{L} \left(n - p + \left(\frac{\delta}{\pi} - 1 \right) \right). \quad (50)$$

As already pointed out, Eq. (48), via Eq. (29), yields the projection $\{a_n^\dagger, b_p\}$, needed to compute $\langle P|\Omega_0\rangle$. Likewise, Eq. (50) yields the projection $\{a_n^\dagger, b_u\}$, needed to compute $\langle U|\Omega_0\rangle$. Equations (48) and (50) show that the substitution $\delta \rightarrow \delta - \pi$ transforms the former into the latter. Since $\sin(\delta)$ only changes sign under the same substitution, we can see that, except for levels close to the band edges, the construction in Fig. 3 maps the single-particle projections needed to compute $\langle P|\Omega_0\rangle$ onto those entering the computation of $\langle U|\Omega_0\rangle$. In other words, the construction establishes the mapping

$$\left| \langle P|\Omega_0\rangle \right|_\delta \mapsto \left| \langle U|\Omega_0\rangle \right|_{\delta-\pi}, \quad (51)$$

where the subscripts indicate that the left- and right-hand terms are calculated with phase shifts δ and $\delta - \pi$, respectively.

Inspection of the right-hand sides of Eqs. (46) and (47) then extends the mapping to the sums \mathcal{P}_P and \mathcal{P}_U , namely,

$$\mathcal{P}_{P,\delta}(t) \mapsto \mathcal{P}_{U,(\delta-\pi)}(t). \quad (52)$$

The fidelity, given by Eq. (45), results from the interference between two similar photoemission processes with distinct threshold energies, split by ϵ_B . The first process involves excitations to the plugged final states, has a lower threshold energy E_P and is described by the Doniach-Sunjc law:

$$\left| \mathcal{P}_{P,\delta} \right|^2 \propto (\omega_\tau t)^{-\alpha}. \quad (53)$$

The second one comprises excitations to the unplugged states, has threshold energy $E_U = E_P + \epsilon_B$ and obeys a different power law,

$$\left| \mathcal{P}_{U,(\delta-\pi)} \right|^2 \propto (\omega_\tau t)^{-\beta}, \quad (54)$$

where

$$\beta \equiv 2 \left(\frac{\delta}{\pi} - 1 \right)^2 \quad (55)$$

is the Nozières-De Dominicis exponent [46].

In the phase-shift range of interest, $0 < \delta/\pi < 1/2$, the exponent β always exceeds α . Consequently, the contribution from $\mathcal{P}_{U,(\delta-\pi)}$ to the fidelity dies out faster, and so does the amplitude of the interference between the two processes. The partition of the final eigenstates into plugged and unplugged states thus explains the damping of the oscillations in Fig. 1. The algebraic approach in the following section confirms this argument.

C. Analytical Results

Appendix A treats Eq. (19) analytically, on the basis of two approximations that become reliable at large times: (i) in the initial Hamiltonian ($K = 0$) the energy splitting Δ_L between neighboring levels is assumed to be uniform throughout the conduction band; (ii) in the final Hamiltonian ($K < 0$), the conduction-band levels above the bound state are assumed to be uniformly phase-shifted. A closed expression for the time-dependent fidelity is derived:

$$\mathcal{F}(t) = \frac{1 + \mathcal{R}_t^2 + 2\mathcal{R}_t \cos(\omega_B t + \vartheta_t)}{(1 + Q)^2} \mathcal{T}_t^{-\alpha} \quad (56)$$

where

$$\mathcal{T}_t \equiv \exp \left(\int_0^{\pi\omega_\tau t} \frac{1 - \cos(x)}{x} dx \right), \quad (57)$$

$$\mathcal{R}_t \equiv Q \mathcal{T}_t^{-\frac{\beta-\alpha}{2}} \quad (58)$$

$$\vartheta_t \equiv \frac{\beta - \alpha}{2} \text{Si}(\pi\omega_\tau t), \quad (59)$$

and

$$Q \equiv \frac{\langle \Omega_U | \Omega_0 \rangle^2}{\langle \Omega | \Omega_0 \rangle^2} \quad (60)$$

where $|\Omega\rangle$ is the ground state of the final Hamiltonian, and $|\Omega_U\rangle$ is the lowest-energy unplugged eigenstate.

The right-hand side of Eq. (60) depends only on the phase shift δ . To show this, we recall that L is equal to the number of conduction electrons. Thus, the denominator of the fraction on the right-hand side is $AL^{-\alpha/2}$, where the prefactor A is independent of L , although dependent on δ [54]. The substitution $\delta \rightarrow \delta - \pi$ transforms α into β . At the same time, it maps the plugged state $|\Omega\rangle$ to the corresponding unplugged state $|\Omega_U\rangle$. Therefore, given that the denominator is $L^{-\alpha/2}$, the numerator must be $BL^{-\beta/2}$, where B is also independent of L , and it follows that $Q = B/A$. It also follows that $Q \mapsto 1/Q$ under $\delta \rightarrow \delta - \pi$.

As mentioned above, Eq. (56) is an algebraic statement of the conclusions drawn in Sec. III B 4. To bring this point home, we define the function

$$\mathcal{P}_{P,\delta}(t) \equiv \frac{1}{1+Q} \mathcal{T}_t^{-\frac{\alpha}{2}} e^{-i\frac{\alpha}{2}} \text{Si}(\pi\omega_\tau t), \quad (61)$$

and then recall that the transformation $\delta \rightarrow \delta - \pi$ implies $\alpha \mapsto \beta$, $\mathcal{P}_{P,\delta} \mapsto \mathcal{P}_{U,(\delta-\pi)}$ and $Q \mapsto 1/Q$. Equation (61) is therefore transformed to

$$\mathcal{P}_{U,(\delta-\pi)}(t) \equiv \frac{Q}{1+Q} \mathcal{T}_t^{-\frac{\beta}{2}} e^{-i\frac{\beta}{2}} \text{Si}(\pi\omega_\tau t), \quad (62)$$

which with the help of Eqs. (58) and (59) can be written as

$$\mathcal{P}_{U,(\delta-\pi)}(t) \equiv \frac{\mathcal{R}_t}{1+Q} e^{-i\vartheta_t} \mathcal{T}_t^{-\frac{\alpha}{2}} e^{-i\frac{\alpha}{2}} \text{Si}(\pi\omega_\tau t). \quad (63)$$

Substitution of $\mathcal{P}_{P,\delta}(t)$ for \mathcal{P}_P and of $\mathcal{P}_{U,(\delta-\pi)}(t)$ for \mathcal{P}_U on the right-hand side of Eq. (45) then yields Eq. (56).

The solid blue line in Fig. 1 represents Eq. (56). For $\omega_\tau t > 15$, the agreement with the numerical data is excellent. The discrepancies at smaller times, most prominent near $\omega_\tau t = 2$, are due to the approximations supporting the derivation of the analytical result, which become accurate for $\omega_\tau t \gg 1$.

Under this condition, Eq. (57) admits simplification. Evaluation of the definite integral on the right-hand side yields

$$\mathcal{T}_t(t) = \exp(\gamma + \log(\pi\omega_\tau t) - \text{Ci}(\pi\omega_\tau t)), \quad (64)$$

where γ is Euler's constant.

For large values of its argument, the cosine integral on the right-hand side is $\mathcal{O}((\omega_\tau t)^{-1})$ and can be withdrawn. Under this approximation, Eq. (64) reads

$$\mathcal{T}_t = e^\gamma \pi\omega_\tau t, \quad (65)$$

which reduces Eq. (56) to the expression

$$\mathcal{F}(t) = \frac{(\pi e^\gamma)^{-\alpha}}{(1+Q)^2} \left(1 + \mathcal{R}_t^2 + 2\mathcal{R}_t \cos(\omega_B t + \vartheta_t) \right) (\omega_\tau t)^{-\alpha}. \quad (66)$$

Equation (56) explains the damping in the inset of Fig. 1. Division of the fidelity by the last factor on its right-hand side yields the ordinate of the inset plot:

$$(\omega_\tau t)^\alpha \mathcal{F}(t) = \frac{(\pi e^\gamma)^{-\alpha}}{(1+Q)^2} \left(1 + \mathcal{R}_t^2 + 2\mathcal{R}_t \cos(\omega_B t + \vartheta_t) \right). \quad (67)$$

On the right-hand side of Eq. (67), the trinomial within parentheses is a law-of-cosines sum of two vectors with magnitudes unity and \mathcal{R}_t whose phases differ by $\omega_B t + \vartheta_t$. The sum oscillates with frequency ω_B and amplitude $2\mathcal{R}_t$. From the definition (58) and Eq. (65) we can see that \mathcal{R}_t vanishes as $\omega_\tau t \rightarrow \infty$. The decay of \mathcal{R}_t abates the oscillations.

$\mathcal{P}_{P,\delta}$ is the contribution of the plugged states to the fidelity, and so $|\mathcal{P}_{P,\delta}|^2$ follows the Doniach-Sunjic power law [47]. Likewise, $\mathcal{P}_{U,(\delta-\pi)}$ is the contribution of the unplugged states, and $|\mathcal{P}_{U,(\delta-\pi)}|^2$ decays in proportion to the Nozières-De Dominicis power law [46]. The energies of the plugged and unplugged states differ ϵ_B ; their phases differ by $\omega_B t$. Therefore, instead of adding up to $|\mathcal{P}_{P,\delta}|^2 + |\mathcal{P}_{U,(\delta-\pi)}|^2$, the two contributions interfere. The interference gives rise to the oscillations in Fig. 1. The more rapid decay (Nozières-De Dominicis-like) of $\mathcal{P}_{U,(\delta-\pi)}$ relative to the (Doniach-Sunjic-like) decay of $\mathcal{P}_{P,\delta}$ accounts for the damping of the oscillations.

To reinforce this interpretation with numerical evidence, consider now the individual contributions $\mathcal{F}_P(t) \equiv |\mathcal{P}_P(t)|^2$ and $\mathcal{F}_U(t) \equiv |\mathcal{P}_U(t)|^2$, of the plugged and unplugged eigenstates, to the fidelity. To determine them, notice that the operator $b_{-L} b_{-L}^\dagger$ projects $|\Psi_t\rangle$ upon the subset of unplugged eigenstates; accordingly, the following expression determines the unplugged component:

$$\mathcal{F}_U(t) = \left| \left\langle \Psi_0 \left| b_{-L} b_{-L}^\dagger \right| \Psi_t \right\rangle \right|^2. \quad (68)$$

The matrix element on the right-hand side of Eq. (68) can be rewritten as

$$\left\langle \Psi_0 \left| b_{-L} b_{-L}^\dagger \right| \Psi_t \right\rangle = \langle \emptyset | a_{-1} \dots a_{-L} b_{-L} b_{-L}^\dagger a_{-L}^\dagger(t) \dots a_{-1}^\dagger(t) | \emptyset \rangle, \quad (69)$$

which is analogous to Eq. (32) and can hence be evaluated by the procedure in Sec. III B 2.

The plugged component is given by the expression

$$\mathcal{F}_P(t) = \left| \left\langle \Psi_0 \left| b_{-L}^\dagger b_{-L} \right| \Psi_t \right\rangle \right|^2, \quad (70)$$

since $b_{-L}^\dagger b_{-L}$ projects $|\Psi_t\rangle$ upon the subset of plugged eigenstates. To compute $\mathcal{F}_P(t)$, therefore, notice taken that $b_{-L}^\dagger b_{-L} = 1 - b_{-L} b_{-L}^\dagger$, we write the matrix element on the right-hand side of

Eq. (69) as

$$\langle \Psi_0 | b_{-L}^\dagger b_{-L} | \Psi_t \rangle = \langle \Psi_0 | \Psi_t \rangle - \langle \Psi_0 | b_{-L} b_{-L}^\dagger | \Psi_t \rangle, \quad (71)$$

which shows that the right-hand side of Eq. (70) can be extracted directly from Eqs. (32) and (69).

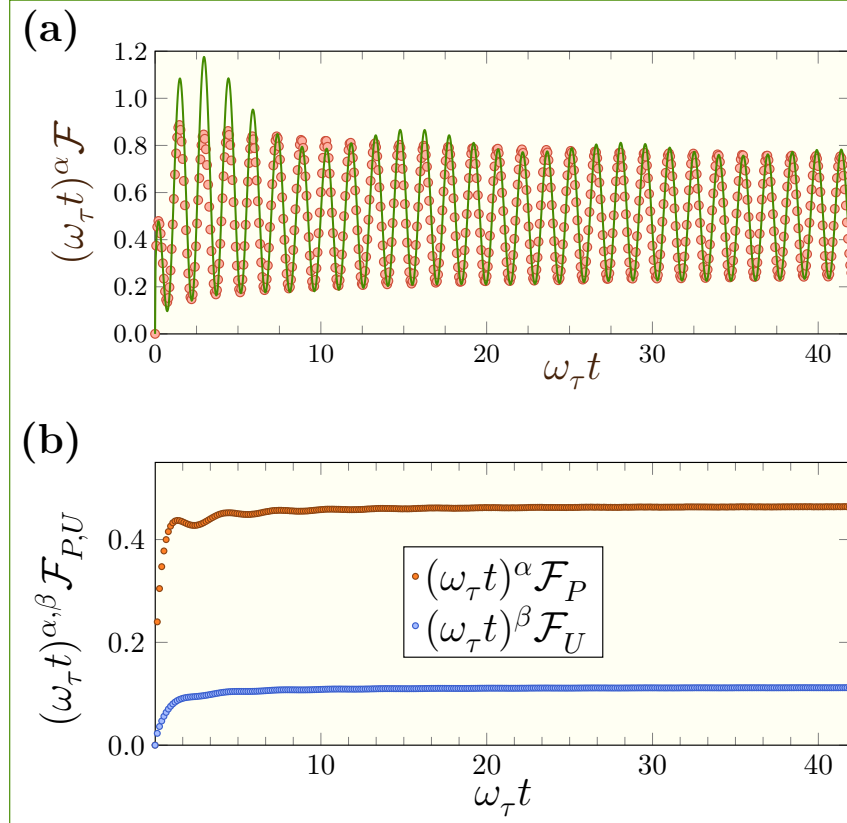


FIG. 4. (a) Comparison between analytical and numerical results for the fidelity. The filled orange circles are the numerical data resulting from straightforward diagonalization of the tight-binding Hamiltonian (1) for $K = -5\tau$ and $2L = 5,000$. The solid green curve represents Eq. (56). For viewing convenience, the analytical and numerical results have been divided by the Doniach-Sunjic law, with α defined by Eq. (40). (b) Absolute values squared of the plugged and unplugged contributions to the fidelity, defined by Eqs. (46) and (47), respectively, computed numerically from Eq. (69) and (71). The plugged and unplugged contributions \mathcal{F}_P and \mathcal{F}_U , represented by the filled orange and blue circles, are divided by the Doniach-Sunjic and Nozières-De Dominicis asymptotic expressions, with exponents defined by Eqs. (40) and (55), respectively.

Figure 4(a) displays the time dependence of the fidelity for $K = -5\tau$. The filled orange circles and the solid green line show the numerical and analytical results, respectively, for $\mathcal{F}(t)$ multiplied by $(\omega_\tau t)^\alpha$. In analogy to Fig. 1, the numerical data practically coincide with Eq. (56) for $\omega_\tau t > 10$. The phase shift $\delta = 0.437\pi$ is close to $\pi/2$, and therefore reduces the exponent on the right-hand

side of Eq. (63), which controls the damping of the oscillation. Therefore, in contrast to Fig. 1 and in striking contrast to Fig. 5 below, the damping is barely perceptible here.

Panel (b) displays the plugged and unplugged components of the fidelity, represented by the orange and blue circles, respectively. The filled orange circles represent $\mathcal{F}_P(t) = \left| \mathcal{P}_P(t) \right|^2$ amplified by the factor $(\omega t)^\alpha$ for $K = -5\tau$; the rapid ascension to a constant verifies conformity to the Doniach-Sunjic law. Similarly, the filled blue circles verify that $\mathcal{F}_U(t) = \left| \mathcal{P}_U(t) \right|^2$ follows the Nozières-De Dominicis law at large times. The disparity between the vigorous oscillations in panel (a) and the dull behavior in (b) is manifest evidence of interference between the transitions to the plugged and unplugged eigenstates.

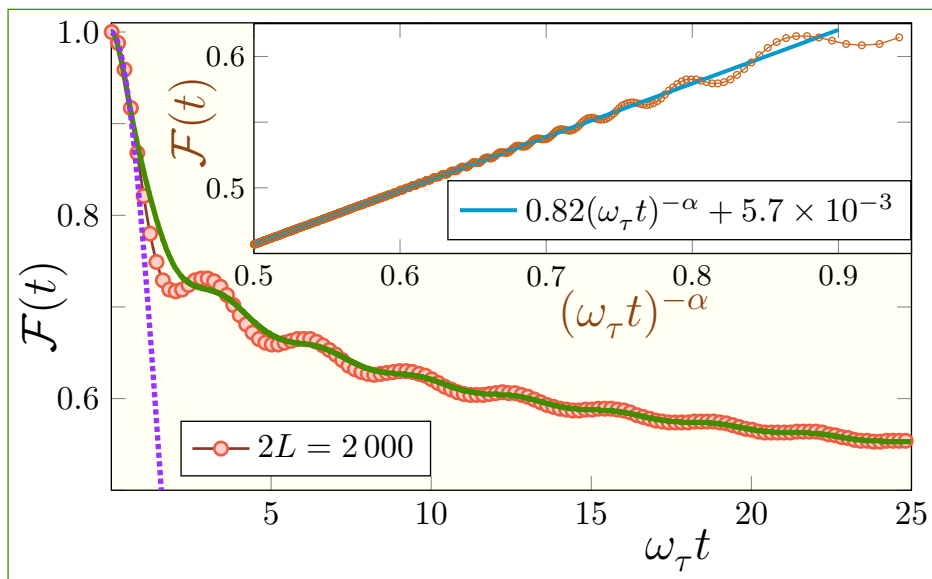


FIG. 5. Fidelity as a function of time for the tight-binding Hamiltonian with 2000 sites and attractive potential $K = -\tau$ (phase shift $\delta = \pi/4$). The filled orange circles, dotted purple line and solid green line represent the numerical data, Eq. (12), and Eq. (56), respectively. The inset displays the fidelity as a function of $(\omega t)^{-\alpha}$, to show adherence to the Doniach-Sunjic law as the contribution from the unplugged states vanishes. The straight cyan line is a least-squares regression showing that the fidelity approaches the residual constant $c_{\text{res}} = 5.7 \times 10^{-3}$ as $\omega_\tau t \rightarrow \infty$, in agreement with Eqs. (19) and (20).

Figure 5 shows the time dependence of the fidelity for a weaker potential $K = -\tau$. The corresponding phase shift in Eq. (83) is $\delta = \pi/4$. As in Fig. 1, there is agreement with the dashed purple line that represents Eq. (12) at very short times only. At long times, Eq. (66) describes the fidelity well, as the solid green line indicates. The relatively small δ bars transition to unplugged eigenstates and reduces the ratio Q in Eq. (60). Since \mathcal{R}_t is proportional to Q , the amplitude $2\mathcal{R}_t$ of the oscillations becomes much smaller than in Fig. 1. Furthermore, while the exponent

$-(1 - 2\delta/\pi)$ on the right-hand side of Eq. (58) was -0.295 for $K = -2\tau$, it is now $-1/2$, which accounts for the rapid dampening of the oscillations.

The inset plots the numerical data as a function of $(\omega_\tau \tau)^{-\alpha}$, to exhibit the behavior over a wider time interval. The oscillations die out as $\omega_\tau t$ grows and, as expected from Eq. (19), the fidelity approaches a small constant. That constant subtracted, the agreement between the filled circles and the Doniach-Sunjić law becomes impeccable at large $\omega_\tau t$, as the straight cyan line shows.

IV. RENORMALIZATION-GROUP APPROACH

Three integers $\zeta \geq 0$, $\lambda > 1$, and $\theta \equiv \log(w)/\log(\lambda)$ ($w \in \mathbb{N}$) parametrize the eNRG construction, which starts with the $L \rightarrow \infty$ tight-binding lattice and divides it into an infinite chain of cells, or intervals. The first ζ intervals \mathcal{C}_ℓ^ζ ($\ell = 1, \dots, \zeta$) contain a single site each. The following interval \mathcal{C}_0 starts a succession \mathcal{C}_n ($n = 0, 1, \dots$), each member of which encompasses $w\lambda^n$ sites. For each cell \mathcal{C}_n , a linear combination of the pertinent operators c_ℓ then defines a normalized Fermi operator f_n [50].

A. Discretized Hamiltonian

Along with the c_ℓ ($\ell = 0, 1, \dots, \zeta$), the f_n ($n = 0, 1, \dots$) form a basis, upon which the model Hamiltonian is projected. The projection brings Eq. (2) to the form [47]

$$\mathcal{H}_K^{\lambda, \zeta, \theta} = \left(\tau \sum_{\ell=0}^{\zeta-1} c_\ell^\dagger c_{\ell+1} + \tau c_\zeta^\dagger f_0 + \sum_{n=0}^{\infty} \tau_n f_n^\dagger f_{n+1} + H. c. \right) + K c_0^\dagger c_0, \quad (72)$$

where

$$\tau_n = \tau \lambda^{-n - \theta - \frac{1}{2}}, \quad (73)$$

with the definition

$$\theta \equiv \frac{\log(w)}{\log(\lambda)}. \quad (74)$$

The coefficients τ_n ($n = 0, 1, \dots$) in Eq. (73) decay exponentially with n . To compute the fidelity at time t , therefore, it is safe to truncate the infinite series on the right-hand side of Eq. (73) at $n = \mathcal{N}$, where \mathcal{N} is the smallest integer such that

$$\frac{\tau_{\mathcal{N}} t}{\hbar} < \eta, \quad (75)$$

where $\eta \ll 1$ is a fixed dimensionless parameter that controls the accuracy of the approximation.

Given t , a truncated, scaled Hamiltonian $\mathcal{H}_K^\mathcal{N}$ is then defined by the equality

$$\mathcal{D}_\mathcal{N} \mathcal{H}_K^\mathcal{N} = \left(\sum_{\ell=0}^{\zeta-1} \tau c_\ell^\dagger c_{\ell+1} + \tau c_\zeta^\dagger f_0 + \sum_{n=0}^{\mathcal{N}-1} \tau_n f_n^\dagger f_{n+1} + H. c. \right) + K c_0^\dagger c_0. \quad (76)$$

Here

$$\mathcal{D}_\mathcal{N} \equiv \tau \lambda^{-\mathcal{N}-1/2}, \quad (77)$$

is the smallest coefficient $\tau_{n=\mathcal{N}}$ for $\theta = 0$.

This scaling ensures that the spectrum of $\mathcal{H}_K^\mathcal{N}$ consists of positive eigenvalues ranging approximately from unity to $2\lambda^{\mathcal{N}+1/2}$ and negative eigenvalues ranging from -1 to $-2\lambda^{\mathcal{N}+1/2}$. Equation (77) reduces (75) to the inequality

$$\frac{\mathcal{D}_\mathcal{N} t}{\hbar} < \eta. \quad (78)$$

The fidelity $\mathcal{F}_{\zeta,\theta}(t)$ can be computed from Eq. (76) along two alternative paths: the many-body approach in Sec. III B 1 or the more efficient single-particle procedure in Sec. III B 2. Either alternative calls for diagonalization of the square matrix of dimension $\mathcal{N} + \zeta + 1$ representing the Hamiltonian $\mathcal{H}_K^\mathcal{N}$. Condition (75), with $\tau_\mathcal{N}$ given by Eq (73), shows that the truncation number \mathcal{N} grows logarithmically with t , a dependence that contrasts with the linear growth of the tight-binding lattice in Sec. III. The computational cost of an eNRG run covering a given time interval is therefore substantially smaller than that of a tight-binding computation of $\mathcal{F}(t)$ in the same time range. Section III B 4 will present examples.

B. Single-particle spectrum

With $K = 0$, the right-hand side of Eq. (76) is particle-hole symmetric, and so is the resulting single-particle spectrum. Given ζ it is convenient to choose \mathcal{N} of the opposite parity, so that $\mathcal{N} + \zeta + 1$ is an even number, henceforth denoted $2M$. Of the single-particle eigenvalues, M will be positive and M , negative, then. The same partition results for $K \neq 0$, and the following approximate expressions describes the single-particle eigenvalues [50]

$$E_j^\pm(K) = \pm \tau \lambda^{2(j-1)} - \theta \pm \frac{2\delta}{\pi} \quad (j = 1, 2, \dots, M), \quad (79)$$

with the same phase shift δ , given by Eq. (26).

Equation (79) is accurate for the eigenvalues in the range $\mathcal{D}_N \ll \mathcal{D}_N |E_j| \ll \tau$. The inaccuracy grows with j and deviations of a few percent become visible close to the upper limit. For negative K , as $|K|$ grows past 2τ , the lowest eigenvalue E_{-M} splits off the bottom of the conduction band. For $K < -2\tau$,

$$\mathcal{D}_N E_{-M} \approx K + \frac{\tau^2}{K}. \quad (80)$$

We will associate the Fermi operators $g_{j\pm}$ and $h_{j\pm}$ ($j = 1, 2, \dots, M$) with the single-particle eigenstates corresponding to the eigenvalues $E_j^\pm(K)$ and $E_j^\pm(0)$ of the final and initial Hamiltonians, respectively.

Although the discretization parameters λ and w were defined as integers, Eqs. (72) and (73) can be rigorously extended to real $\lambda \gg 1$ and θ [50]. Since Eq. (72) reduces to the tight-binding Hamiltonian (2) for $\lambda = 1$, to justify the discretization one must show that the physical properties resulting from the spectrum of (72) converge rapidly to the continuum limit as $\lambda \rightarrow 1$.

C. Computation of the fidelity

The analysis leading from Eq. (32) to Eq. (36) can be repeated, with the discretized Hamiltonian (76) substituted for the tight-binding Hamiltonian (24). The projection between the initial ground state and the time-dependent state can then be computed from an expression analogous to Eq. (35),

$$\langle \Psi_t | \Psi_0 \rangle = \det \underline{\underline{M}}^{\mathcal{N}}(t), \quad (81)$$

where the matrix elements of the $M \times M$ matrix $\underline{\underline{M}}^{\mathcal{N}}(t)$ are

$$\underline{\underline{M}}_{m,n}^{\mathcal{N}}(t) = \sum_p \left\{ h_m, g_p^\dagger \right\} e^{-i\epsilon_p^\pm t/\hbar} \left\{ g_p, h_n^\dagger \right\}. \quad (82)$$

1. Numerical results

Numerical diagonalization of the initial and the final Hamiltonians $\mathcal{H}_0^{\mathcal{N}}$ and $\mathcal{H}_K^{\mathcal{N}}$ for a specific set of eNRG parameters λ , ζ , and θ and adequately chosen truncation number \mathcal{N} , followed by substitution of the right-hand side of Eq. (81) for the projection on the right-hand side of Eq. (3) yields the *raw* fidelity

$$\mathcal{F}_{\zeta,\theta}(t) = |\det \{ \underline{\underline{M}}^{\mathcal{N}}(t) \}|^2. \quad (83)$$

The eNRG method inherits a trait of the NRG procedure and intersperses plots of physical properties with non-physical oscillations. Thermodynamical properties computed with $\lambda > 1$ display sinusoidal functions of the temperature added to the exact thermal dependence, that is, the thermal dependence that a calculation with $\lambda = 1$ would produce. In this case, averaging two successive ζ 's and a few θ 's in the interval $-1 \leq \theta \leq 1$ is enough to eliminate these artifacts [50].

The computation of the time-dependent fidelity poses a more complex problem because it involves not one but two discrete spectra—those of the initial and final Hamiltonians. Instead of the uniform energy difference between the plugged and unplugged many-body excitations in Fig. 2 we find a variety of splittings, the dispersion of which increases with the discretization parameter λ . The resulting fidelity is the sum of a number of artificially distinct frequencies. Gone is the harmony of the damped oscillations in Figs. 1, 4 and 5.

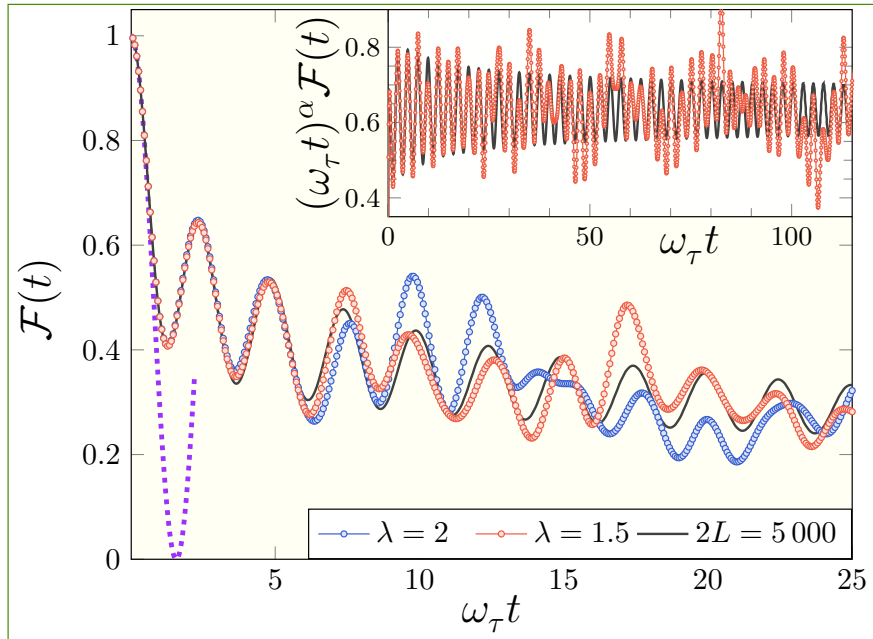


FIG. 6. eNRG results for the raw fidelity, given by Eq. (83), for $K = -2\tau$ as a function of time scaled by $\omega_\tau \equiv \tau/\hbar$. The filled orange and blue circles represent the time dependence of the raw fidelity for $\lambda = 1.5$ and 2, respectively, both computed with $\zeta = 3$ and $\theta = 0$. The dashed purple line is Eq. (12), accurate at short times only. The solid black line is the fidelity for the tight-binding Hamiltonian (24) with $2L = 5000$ lattice sites. The inset compares the data for $\lambda = 1.5$ averaged over $\zeta \in \{3, 4\}$ (filled orange circles) with the fidelity for the tight-binding Hamiltonian (solid black line). The orange circles show that, divided by the Doniach-Sunjic power law $(\omega_\tau t)^{-\alpha}$, the raw fidelity fluctuates about a constant at long times.

As an illustration, Fig. 6 shows the fidelity resulting from Eq. (79) for $\lambda = 1.5$ (filled orange circles) and 2 (filled blue circles), with $K = -2\tau$, $\zeta = 3$ and $\theta = 0$ in both cases. The discretized

Hamiltonians were truncated at $\mathcal{N} = 34$ ($\lambda = 1.5$) and 20 ($\lambda = 2$), respectively, to satisfy (75) with $\eta = 10^{-3}$ up to $\omega_\tau t = 1000$. All the computations in this section were carried out with truncation numbers sufficiently large to satisfy that inequality up to the same maximum time. For comparison, the solid black curve shows the essentially exact fidelities calculated from the spectrum of the tight-binding Hamiltonian with $2L = 5000$ lattice sites.

Like the solid curve, the eNRG curves oscillate with frequency ω_B . However, undulations with substantially smaller frequencies modulate the plots. These are beat frequencies due to the aforementioned nonuniform energy splittings in the single-particle spectrum (79) of the truncated Hamiltonian $\mathcal{H}_K^\mathcal{N}$. The unevenness increases with λ . For this reason, beats with different frequencies and amplitudes distinguish the orange curve from the blue one, with the latter deviating more than the former from the black plot.

The inset compares the $2L = 5000$ data with the fidelity computed with $\lambda = 1.5$ and $\theta = 0$, and averaged over $\zeta \in \{3, 4\}$. The two fidelities are multiplied by $(\omega_\tau \tau)^{-\alpha}$, with the exponent (39), to verify compliance with the Doniach-Sunjić power law [47]. Comparison with the orange circles in the main plot shows that averaging on ζ dampens the deviations but does not eliminate them. Similar irregularities remain after averaging longer sequences, with $\zeta \in \{3, 4, 5, 6\}$ (not shown), for example.

In any case, the irregular beats are persistent. With $\zeta \in \{3, 4\}$, for example, the pattern in the main plot is repeated up to the longest time studied $\omega_\tau t = 10000$ (not shown).

At small times, the eNRG procedure is accurate. In the interval $0 \leq \omega_\tau t < 5$, which extends well beyond the validity of the dotted purple line representing Eq. (12) in the main plot, the circles follow the black curve. Outside that range, the orange and blue curves deviate from each other, become irregular, and wobble around the $2L = 5000$ curve.

2. Time scale T_ζ

Why are the computed fidelities independent of λ at small times? This question prompts us to consider the time scales in the eNRG Hamiltonian. Section. III B 3 associated T_L with the smallest energy in the single-particle spectrum of the tight-binding Hamiltonian. The analogous energy in the eNRG approach is $\mathcal{D}_\mathcal{N}$, which defines the time scale $T_\mathcal{N} \equiv \hbar/\mathcal{D}_\mathcal{N}$. At times $t \ll T_\mathcal{N}$, the energy scales close to $\mathcal{D}_\mathcal{N}$ will contribute insignificantly to the time-evolution operator $\exp(-i\mathcal{D}_\mathcal{N}\mathcal{H}_K^\mathcal{N}t)$; under this condition, $\mathcal{F}(t)$ will be independent of \mathcal{N} , although it will generally vary with λ , θ and ζ .

However, the latter parameter introduces an exception. The first term within parentheses on the right-hand side of Eq. (72) is a segment of the eNRG chain equivalent to a tight-binding lattice of size ζ . Analogy with the discussion of Eq. (38) defines a second characteristic time T_ζ , through the equality

$$\omega_\tau T_\zeta \equiv \zeta. \quad (84)$$

In the interval $0 \leq t < T_\zeta$, the properties of the eNRG Hamiltonian are independent of λ and θ , because they are governed by the energy scales in that segment of the chain, which is not affected by discretization. The independence of λ implies that the fidelities in this interval accurately represent the continuum limit.

The results in Fig. 6 were obtained with $\zeta = 3$, which corresponds to $\omega T_\zeta = 3$. Close inspection shows that the orange and blue circles become distinguishable from each other and from the black line at $\omega_\tau t \approx 3$, that is, $t = T_{\zeta=3}$. The good agreement at smaller times confirms that the eNRG data are reliable over the interval defined by T_ζ .

Figure 7 offers additional evidence. The two panels compare the raw fidelities computed with $\zeta = 100$, $\lambda = 2$, and $\theta = 0$ (orange circles) with the fidelity for the tight-binding Hamiltonian with $2L = 5000$ lattice sites (solid black line). There is perfect agreement until $t = T_\zeta$ ($\omega_\tau t = 100$). Shortly after that, starting at $\omega_\tau t = 105$, the orange circles abruptly deviate from the black line. Analogous comparisons between the eNRG and tight-binding results for the plugged (\mathcal{F}_P) and unplugged (\mathcal{F}_U) components of the fidelity (not shown) ratify this finding and show that, even with the relatively large $\lambda = 2$ and without averaging over θ or ζ , the eNRG procedure yields virtually exact results for $t < T_\zeta$.

Figure 8 extends the comparison to longer times $0 \leq \omega_\tau t < 500$. To enclose that interval in the range $0 < t < T_\zeta$, the fidelities were calculated with $\zeta = 600$. Panel (a) shows excellent agreement between the eNRG results at short times ($\omega_\tau t < 50$) and those derived from the diagonalization of the tight-binding Hamiltonian with $2L = 5000$. At longer times ($\omega_\tau t \lesssim 500$), however, the agreement deteriorates, as panel (b) shows. To identify the origin of the discrepancy, panels (c) and (d) show the contributions of the plugged many-body states to the fidelities divided by the Doniach-Sunjic power law for both Hamiltonians, over different ranges of time. In analogy to panel (a), panel (c) witnesses the excellent agreement between the plugged fidelities at short times ($\omega_\tau t < 40$). Panel (d) expands the vertical axis to zoom in near the $t \rightarrow \infty$ limit, indicated by the dashed black line. The solid blue line representing the results for the tight-binding Hamiltonian rises above the flat brown curve that represents the plugged fidelity for the eNRG Hamiltonian. The

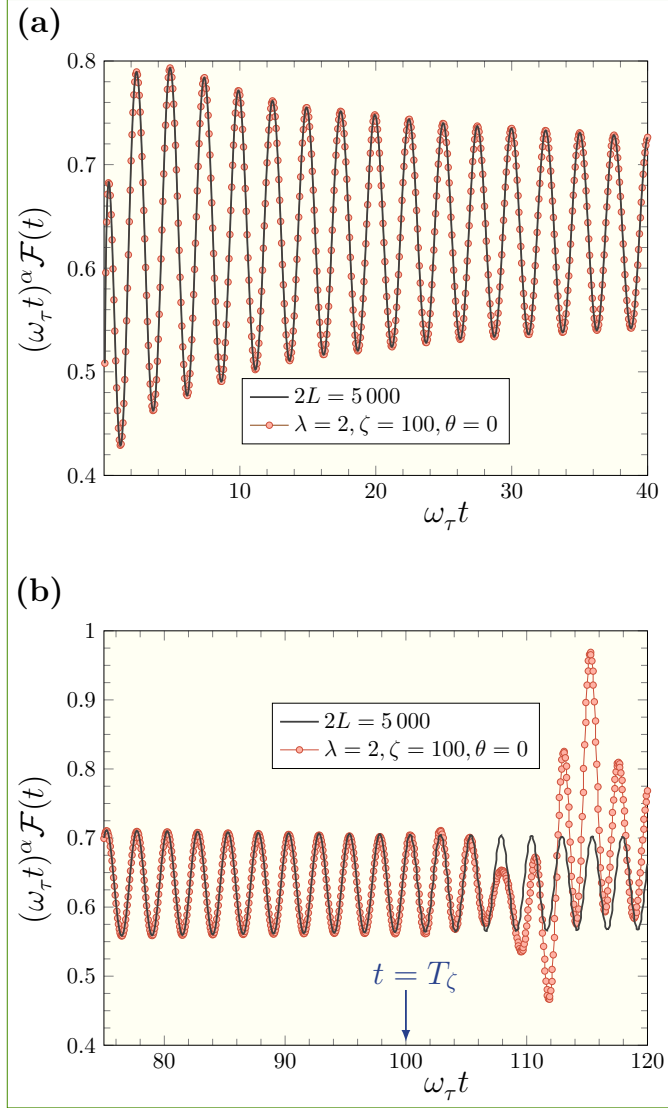


FIG. 7. Comparison between the time-dependent fidelities for the eNRG Hamiltonian with the displayed parameters and the tight-binding Hamiltonian with $2L = 5000$. In the two panels, the filled orange circles show the eNRG data computed with $\mathcal{N} = 19$. The solid black curve is the tight-binding fidelity. For improved resolution, both curves have been scaled by the Doniach-Sunjic power $(\omega_\tau t)^\alpha$. Panel (a), restricted to small times, shows perfect agreement between the orange circles and the black line. Panel (b) covers the vicinity of the characteristic eNRG time T_ζ , identified by the vertical arrow pointing to the horizontal axis. While flawless for $t < T_\zeta$, the agreement deteriorates rapidly as t grows beyond the characteristic time.

disagreement between the blue and brown curves, therefore, exposes a small finite-size effect — one that is nevertheless significant—influencing the fidelities $\mathcal{F}(t)$, $\mathcal{F}_P(t)$, and $\mathcal{F}_U(t)$ (not shown) for the tight-binding Hamiltonian only. Analogous deviations arise in eNRG computations with small ζ , as discussed in the following section.

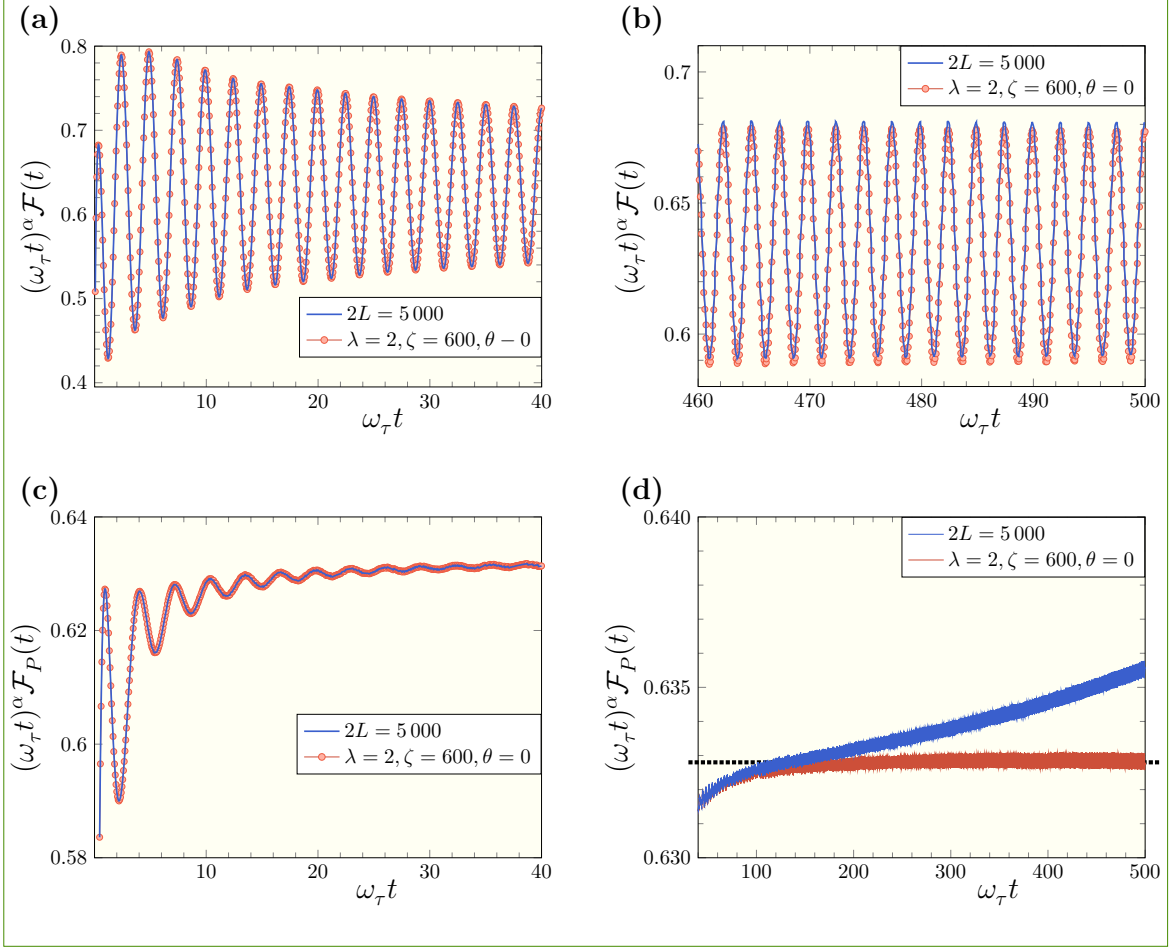


FIG. 8. Comparison between the fidelities for the eNRG and tight-binding Hamiltonians with $K = -2\tau$. The eNRG data were computed with the displayed parameters, and $\mathcal{N} = 21$. The tight-binding results came from the diagonalization that yielded the data in Figs. 6 and 7. Panels (a) and (b) compare the fidelities at short and long times, respectively, to contrast agreement in the former range with small disagreement in the latter. Panels (c) and (d) display the equivalent comparisons for the plugged contributions to the fidelities. Since the product $(\omega_\tau t)^\alpha \mathcal{F}_P(t)$ must approach a constant at long times, panel (d) proves the $\zeta = 600$ eNRG results more precise than the $2L = 5000$ tight-binding data.

3. Smoothed fidelity

As Sec. IV C 2 explained, the eNRG procedure yields essentially exact fidelities in the time range $0 \leq t < T_\zeta$. From the perspective of computational cost, the eNRG method is very efficient. Given a time interval, the effort needed to compute the fidelity is a small fraction of the effort to diagonalize the tight-binding Hamiltonian that yields comparable accuracy. For example, the eNRG run and the diagonalization of the $2L = 5000$ tight-binding Hamiltonian that provided the

data in Fig. 8 demanded 51 seconds and 7100 seconds of CPU time, respectively, on a standard laptop computer.

These considerations refer to our model Hamiltonian, which reduces to two quadratic forms. The diagonalization of a quartic eNRG Hamiltonian would be substantially more demanding computationally. Large ζ 's would make the cost of diagonalizing one such Hamiltonian iteratively [28] prohibitive, because the spectrum of the eNRG Hamiltonian cannot be truncated in the first ζ iterations. In practice, therefore, we are restricted to moderate offsets, that is, ζ 's that are substantially smaller than the time interval of interest. This brings us to the problem of computing $\mathcal{F}(t)$ for $t > T_\zeta$.

In the time domain defined by this inequality, we have to deal with beat frequencies like those in Fig. 6. To this end, following the procedure that has been tested in the computation of thermodynamical and transport properties [50], we average the raw fidelities on a set C_ζ containing $N_\zeta = 2$ consecutive offsets ζ and integrate them over θ to obtain the *smoothed* fidelity:

$$\bar{\mathcal{F}}(t) = \frac{1}{N_\zeta} \sum_{\zeta \in C_\zeta} \int_{-1}^1 \mathcal{F}_{\zeta, \theta} d\theta. \quad (85)$$

Here, we work with $C_\zeta = \{3, 4\}$ and use Simpson's $1/3$ rule with an even number N_θ of intervals to evaluate the integral on the right-hand side of Eq. (85), that is, a set of $N_\theta + 1$ equally spaced points ranging from $\theta = -1$ to $\theta = 1$.

It is instructive to consider the deviations that Simpson's approximation introduces. As Eq. (16) shows, the raw fidelity depends on a set of many-body eigenvalues E_r and eigenvectors that, in turn, depend on the sliding parameter θ . If we let $\Upsilon(\theta)$ denote the average value of the E_r 's that contribute to the right-hand side of that equality, then we can substitute $\Upsilon(\theta)$ for the integration variable on the right-hand side of Eq. (85). With this substitution, the deviation introduced by Simpson's rule is controlled by the differences

$$\Delta\Upsilon_j = \Upsilon(\theta_{j+1}) - \Upsilon(\theta_j) \quad (j = 1, \dots, N_\theta), \quad (86)$$

where the θ_j are the points defining the Simpson integration over θ . Clearly, when the other parameters are fixed, all the $\Delta\Upsilon_j$ decay in an inverse proportion to N_θ .

Figure 9 shows the time-dependent fidelity for $K = -4\tau$, calculated in runs with $N_\theta = 100$ and two discretization parameters: $\lambda = 2$ [panels (a) and (b)] and $\lambda = 1.5$ [panels (c) and (d)]. Each panel compares orange circles representing the smoothed fidelities with a solid black curve that shows the essentially exact fidelity computed by the procedure in Sec. IV C 2 with $\zeta = 600$.

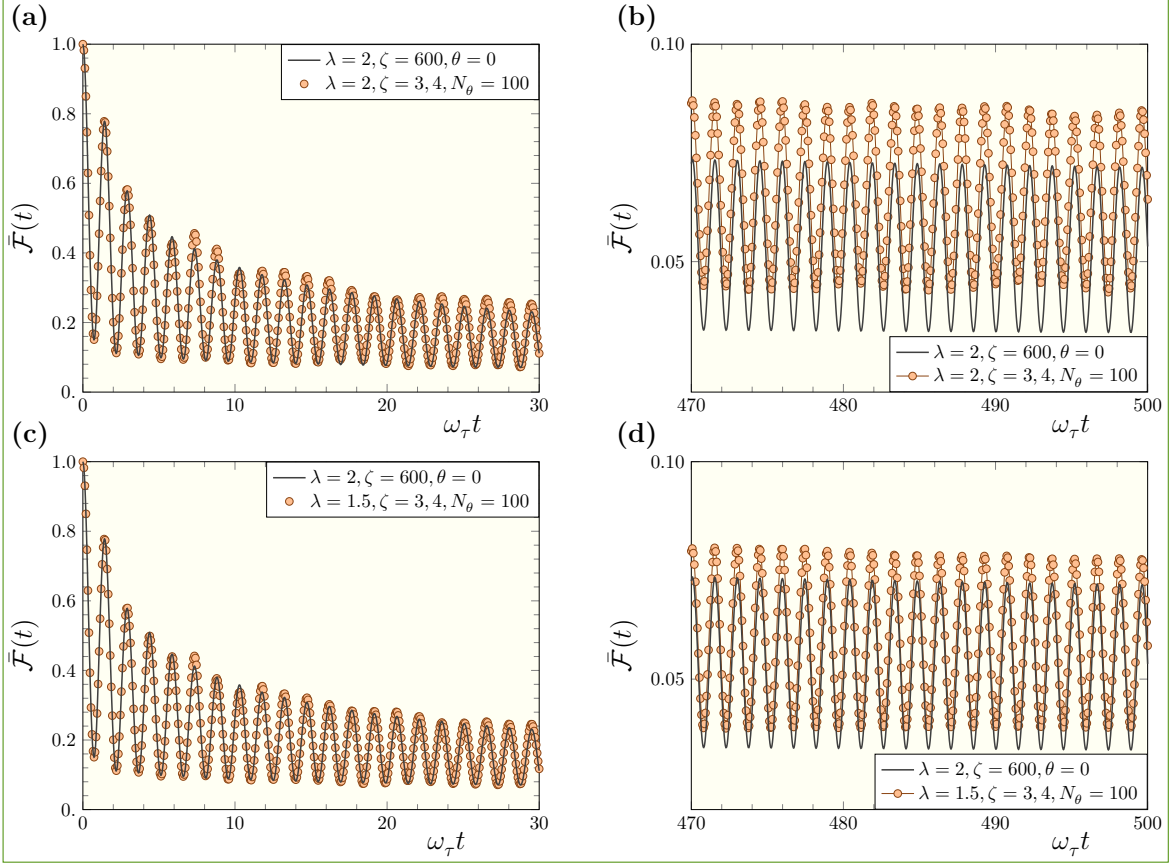


FIG. 9. Comparison between time-dependent fidelities for the potential scattering $K = -4\tau$ computed with distinct sets of eNRG parameters. In each panel, the black curve represents essentially exact data for the fidelity, computed with $\lambda = 2$, $\zeta = 600$, $\theta = 0$, and $\mathcal{N} = 21$, and the filled orange circles represent the smoothed fidelity $\overline{\mathcal{F}}_{\zeta,\theta}$, averaged on $\zeta = 3, 4$ and integrated over θ with $N_\theta = 100$. Panels (a) and (b) show the short- and long-time behaviors, respectively, computed with $\lambda = 2$ and $\mathcal{N} = 22$. Panels (c) and (d) show the equivalent results computed with $\lambda = 1.5$ and $\mathcal{N} = 27$.

At small times [panels (a) and (c)], the circles match the black curve fairly well. At larger times, in panels (b) and (d), substantial deviations arise. Although each curve in these panels oscillates around a constant, the averages and amplitudes of the oscillations drawn by the orange circles are visibly larger than those of the solid black curves.

At the root of these discrepancies are residual contributions analogous to the linear intercept in the inset of Fig. 5. It follows from Eq. (19) that numerically computed fidelities approach the constant c_{res} , defined by (20), as $t \rightarrow \infty$. Likewise, the contributions $\mathcal{F}_P(t)$ [$\mathcal{F}_U(t)$] of the plugged states (unplugged) to the fidelity must approach the corresponding residual values c_{res}^P (c_{res}^U). To confirm these expectations, Fig. 10 shows \mathcal{F}_P as a function of the Doniach-Sunjic function $(\omega\tau t)^{-\alpha}$

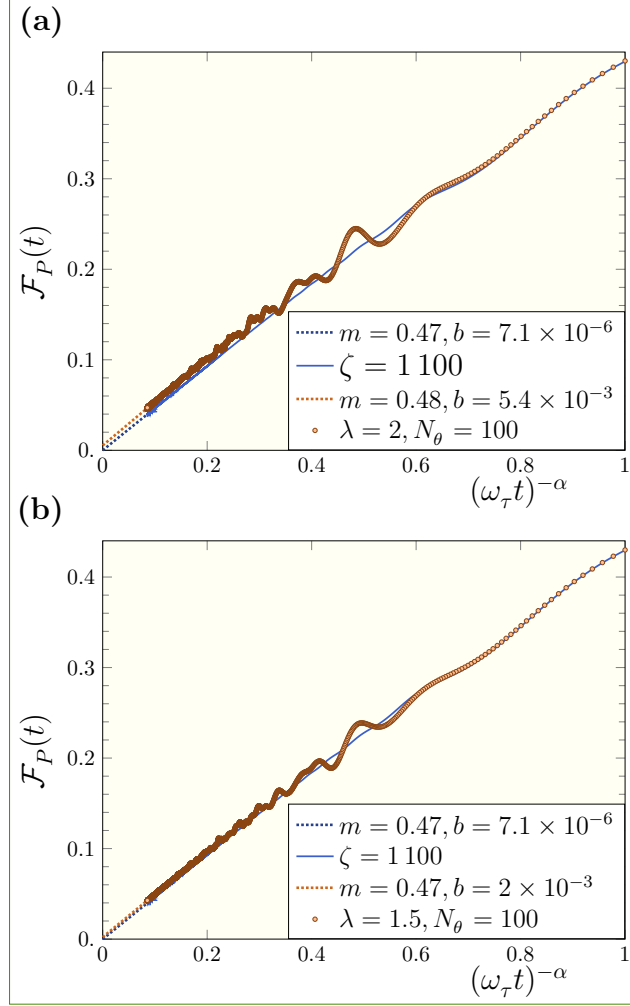


FIG. 10. Comparison between the long-time behaviors of the plugged fidelity for $K = -4\tau$ computed with different sets of eNRG parameters and plotted as functions of the Doniach-Sunjc power law $(\omega t)^{-\alpha}$. In the two panels, the solid blue curve represents essentially exact results for the fidelity, computed with $\lambda = 2$, $\zeta = 1\,100$, $\theta = 0$, and $\mathcal{N} = 23$, while the dotted blue line shows its extrapolation to $t \rightarrow \infty$. The solid orange circles in panel (a) [(b)] represent the plugged fidelity computed with $\lambda = 2$ (1.5), and averaged on $\zeta = 3, 4$ and integrated with $N_\theta = 100$. The dotted orange lines depict the linear extrapolation of the orange curves to $t \rightarrow \infty$.

and the linear extrapolations of \mathcal{F}_P to $t \rightarrow \infty$ for $\lambda = 2$ [panel (a)] and $\lambda = 1.5$ [panel (b)]. As in Fig. 5, the dotted lines representing the linear regressions fit the computed fidelities very well for $\omega_\tau t > 100$, which corresponds to $(\omega_\tau t)^{-\alpha} \approx 0.19$, and the intercepts determine the residual constants, $c_{\text{res}}^P = 5.4 \times 10^{-3}$ for $\lambda = 2$, and $c_{\text{res}}^P = 2.2 \times 10^{-3}$ for $\lambda = 1.5$. For comparison, the two panels also show the fidelity calculated with $\zeta = 1\,100$ and its extrapolation to $t \rightarrow \infty$, which yields a much smaller residual constant, $c_{\text{res}}^P = 7.1 \times 10^{-6}$. The plots of $\mathcal{F}_U(t)$ as a function of the

Nozière-De Dominicis power $(\omega_\tau t)^{-\beta}$ (not shown) yield analogous results.

In summary, the calculated fidelities oscillate about a residual constant c_{RES} at large times. As $t \rightarrow \infty$, the progressive damping of the oscillations brings $\bar{\mathcal{F}}(t)$ to this residual value. Whereas large-offset computations yield very small c_{RES} , the larger residual constants resulting from small-offset, large N_θ runs introduce significant vertical displacements in plots such as those in Fig. 9(b) and Fig. 9(d).

The magnitudes of the discrepancies depend on λ . The differences in panel (d) are substantially smaller than those in panel (b). This indicates that the computed fidelities converge rapidly to the tight-binding ($\lambda = 1$) limit. To monitor this convergence, Secs. IV C 4 and IV C 5 study the dependence of $\bar{\mathcal{F}}(t)$ on the eNRG parameters. For easier comparison, instead of the computed fidelities $\bar{\mathcal{F}}(t)$, we will examine the deviations

$$\Delta\mathcal{F}(t) \equiv \bar{\mathcal{F}}(t) - \mathcal{F}_{\text{ref}}(t), \quad (87)$$

where the reference function $\mathcal{F}_{\text{ref}}(t)$ is the fidelity for $K = -4\tau$ computed with $\lambda = 2$, $\zeta = 1100$, and $\theta = 0$, a parametrical choice that yields essentially exact results in the interval $0 \leq \omega_\tau t < 1000$.

4. Dependence on N_θ

The solid green lines and the orange and blue circles in Fig. 11 show the deviations $\Delta\mathcal{F}(t)$ resulting from eNRG calculations of $\bar{\mathcal{F}}(t)$ for $K = -4\tau$ with $N_\theta = 20, 100$ and 1000 , respectively. The three runs were carried out with $\lambda = 2$ and averaged on $\zeta \in \{3, 4\}$. Panel (a) covers the interval $\omega_\tau t < 50$ and shows three congruent curves. This coincidence is expected, for at a given time t , the uncertainty principle broadens the energies by \hbar/t ; at small times, therefore, the broadening dwarfs the splittings $\Delta\Upsilon$ in Eq. (86). Even the largest ones, associated with $N_\theta = 20$ are much smaller than \hbar/t_{MAX} ($\omega_\tau t_{\text{MAX}} = 50$). In the intermediate time interval depicted in panel (b), the broadening become smaller than the energy splittings $\Delta\Upsilon_j$ for $N_\theta = 20$; the discrepancies between the green line and the circles reflect the deviations caused by Simpson's approximation.

Panel (c) depicts the interval $900 < \omega_\tau t < 950$. Now, the energy uncertainties are smaller than the Υ_j for $N_\theta = 20$ and 100 , but larger than the splittings for $N_\theta = 1000$. Accordingly, the blue circles draw a nearly uniform, small-amplitude oscillation, in contrast with the less regular behavior of the red circles and the prominent swings of the green line.

Altogether, the three panels indicate that, with sufficiently large N_θ —as a rule of thumb, $N_\theta \gtrsim \omega_\tau t$ is needed to compute $\mathcal{F}(t)$ —integration over θ eliminates the spurious oscillations due to

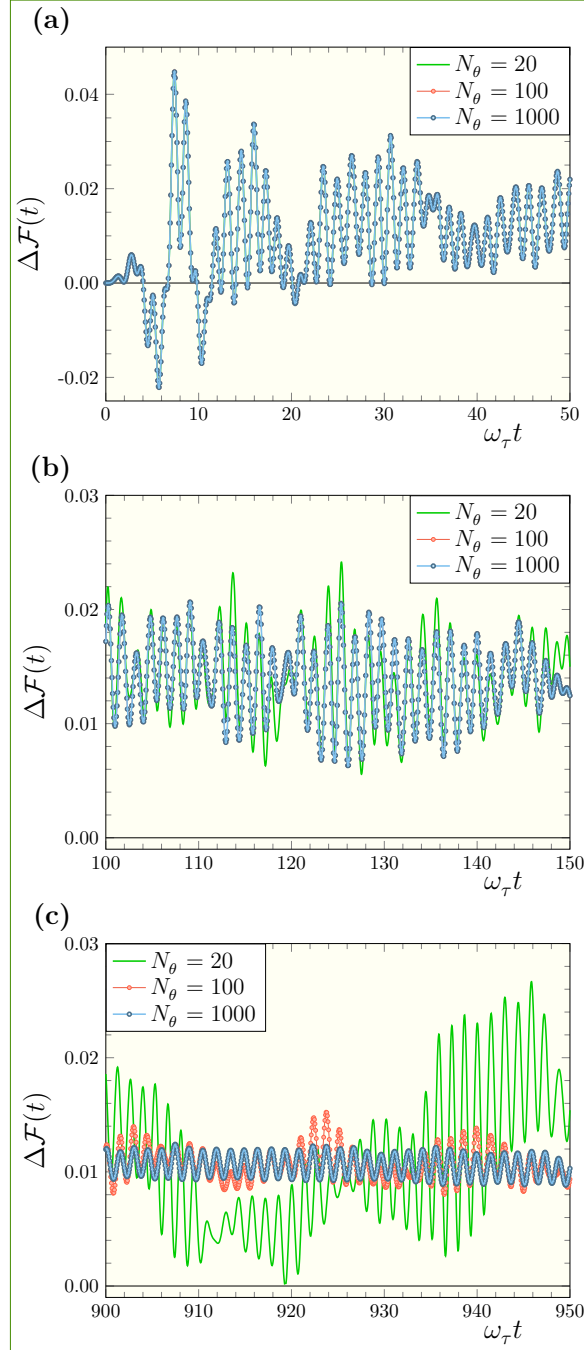


FIG. 11. Deviations of the fidelities computed for $K = -4\tau$ with $\lambda = 2$, averaged on $\zeta \in \{3, 4\}$ and the indicated numbers of θ 's ($N_\theta = 20$, solid green line; $N_\theta = 100$, orange circles; and $N_\theta = 1000$, blue circles) from the essentially exact curve, computed with $\lambda = 2$, $\zeta = 1100$, and $\theta = 0$, at short [panel (a)], medium [panel (b)], and long times [panel (c)].

the nonuniform distribution of the single-particle energy levels in the eNRG procedure; the minute, regular deviations depicted by the blue circles in panel (c) offer especially compelling evidence.

However, the fluctuations in panel (a) defy smoothing, with alternating positive and negative values that can be as large as 5×10^{-2} at small times. The deviations become systematically positive and more harmonic as time increases. These oscillations, drawn by all three curves in panel (a), by the curves calculated with $N_\theta = 100$ and 1 000 in panel (b), and by the curve with $N_\theta = 1\,000$ in panel (c), cannot be attributed to the nonuniformity of the single-particle spectrum.

This identifies two classes of deviations. In the first class are those due to the nonuniformity, which persist indefinitely but can be smoothed out by ζ averaging combined with Simpson integration over θ with sufficiently large N_θ . For easier reference, we will call *persistent* the discrepancies in this class. The fluctuations of the orange curve in the inset of Fig. 6 constitute an example.

The second class comprises deviations that decay but cannot be smoothed out, as best illustrated by the blue circles in Fig. 11. We call them *transitory*. To identify the source of these discrepancies, Sec. IV C 5 compares eNRG data for different discretization parameters.

5. Dependence on λ

As explained in Sec. III B 3, each of the two functions $\bar{\mathcal{F}}(t)$ and $\mathcal{F}_{\text{ref}}(t)$ on the right-hand side of Eq. (87) receives a contribution $\mathcal{F}_P(t)$ from plugged states and a contribution $\mathcal{F}_U(t)$ from unplugged ones. Since $\mathcal{F}_P(t)$ and $\mathcal{F}_U(t)$ behave differently and approach different residual constants at long times, the function $\Delta\mathcal{F}(t)$ depends on all the eNRG parameters.

The most important for our purposes is the dependence on the discretization parameter λ . As mentioned in Sec. IV B, the discretization leading to Eq. (71) is an approximation that can only be justified *a posteriori*. To this end, we must show that the eNRG computation of the physical property of interest converges rapidly to the continuum limit ($\lambda = 1$), so that calculations carried out with discretization parameters compatible with practical considerations of computational cost yield absolute deviations of a few percent or less.

Figure 12 shows the deviations resulting from three eNRG runs for $K = -4\tau$ with distinct discretization parameters: $\lambda = 1.5$ ($\mathcal{N} = 38$, solid blue curve), 2 ($\mathcal{N} = 22$, red), and 3 ($\mathcal{N} = 14$, green). All fidelities were averaged on $\zeta \in \{3, 4\}$ and integrated with $N_\theta = 1\,000$. Panels (a), (b), and (c) in Fig. 11 can be regarded as blow-ups of the red curve in Fig. 12 that expand the intervals $0 \leq \omega_\tau t \leq 50$, $100 \leq \omega_\tau t \leq 150$, and $900 \leq \omega_\tau t \leq 950$, respectively.

In the interval $0 \leq \omega_\tau t \leq 10$, the three curves exhibit relatively large variations. The green curve fluctuates between $\Delta\mathcal{F} = -3 \times 10^{-2}$ and 8×10^{-2} , approximately, the red curve, between $\Delta\mathcal{F} = -2 \times 10^{-2}$ and 4×10^{-2} [cf. Fig. 11(a)], and the blue curve, between $\Delta\mathcal{F} = -2 \times 10^{-2}$

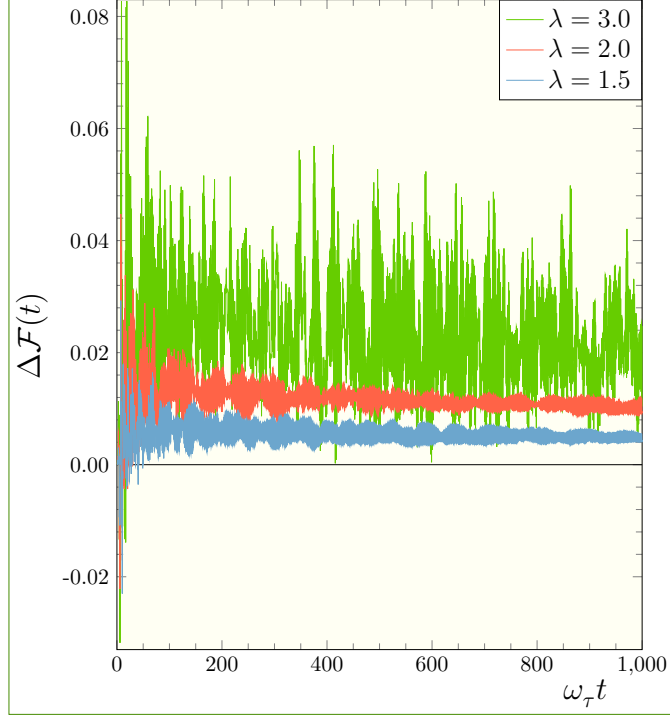


FIG. 12. Deviations of the fidelities computed for $K = -4\tau$ with $\zeta \in \{3, 4\}$, $N_\theta = 1000$, and the indicated discretization parameters from the essentially exact results obtained with $\lambda = 2$, $\zeta = 1100$, $\theta = 0$, and $\mathcal{N} = 23$.

and 3×10^{-2} . Fluctuations become more regular as $\omega_\tau t$ grows and their amplitudes decrease. At the end of the interval, $\omega_\tau t \approx 1000$, each curve is centered on a positive constant, approximately equal to 2×10^{-2} for $\lambda = 3$, 1×10^{-2} for $\lambda = 2$, and 5×10^{-3} for $\lambda = 1.5$. The amplitudes also decay as λ decreases, at all times. Thus, the eNRG procedure with $\lambda = 1.5$ produces accurate smoothed fidelities, except for the short time interval $0 \leq \omega_\tau t < 200$. Outside that range, the absolute deviations never reach 1×10^{-2} .

In the light of renormalization-group theory, Fig. 12 helps to identify the source of transitory fluctuations. The substantial deviations resulting from the run with $\lambda = 3$ point to operators artificially introduced by the eNRG discretization. Given the Hamiltonian $\mathcal{H}_K^\mathcal{N}$, the mapping $\mathbb{T}[\mathcal{H}_K^\mathcal{N}] = \mathcal{H}_K^{\mathcal{N}+2}$ defines the renormalization-group transformation \mathbb{T} [35]. As \mathcal{N} increases, $\mathcal{H}_K^\mathcal{N}$ approaches a fixed-point \mathcal{H}_δ^* of the transformation, characterized by the phase shift in Eq. (26) [55]. At given \mathcal{N} , the difference $\delta_{\mathcal{H}}^\mathcal{N} = \mathcal{H}_K^\mathcal{N} - \mathcal{H}_\delta^*$ can be written as a linear combination of charge-conserving operators in the space spanned by the many-body eigenstates of $\mathcal{H}_K^\mathcal{N}$:

$$\delta_{\mathcal{H}}^\mathcal{N} = \sum_{m=0}^{\mathcal{M}} w_m^\mathcal{N} \mathcal{O}_m, \quad (88)$$

where \mathcal{M} is the number of all such operators that can be constructed.

Equation (88) is in diagonal form. The \mathcal{O}_m on the right-hand side are eigenoperators of the transformation \mathbb{T} , termed *irrelevant* because the corresponding eigenvalues are smaller than unity. As $\mathcal{N} \rightarrow \infty$, the coefficients $w_m^{\mathcal{N}} \rightarrow 0$ and the right-hand side of Eq. (88) vanishes.

The eigenvalues and eigenvectors of the fixed-point Hamiltonian depend on the discretization parameters λ , ζ , and θ , and so do the physical properties derived from them. The time dependence of the raw fixed-point fidelity shows artificial oscillations, analogous to those in Fig. 6, which disappear after $\mathcal{F}_{\zeta,\theta}(t)$ is smoothed over ζ and θ . More important in the context of the present discussion, the residual constant defined by Eq. (20), which vanishes in the continuum, increases monotonically with λ . The linear regressions in Fig. 10 offer illustrations.

Figure 12 offers additional evidence. At long times ($\omega_\tau t > 800$), each curve fluctuates about the residual constant c_{res} associated with the corresponding discretization parameter λ . The blue, orange and green curves, calculated with $\lambda = 1.5, 2$ and 3 , fluctuate about $c_{\text{res}} = 5 \times 10^{-3}, 1 \times 10^{-2}$ and 2×10^{-2} , respectively.

The irrelevant operators in $\mathcal{H}_K^{\mathcal{N}}$ account for the large fluctuations at smaller times. The decay of the irrelevant operators with \mathcal{N} defines a hierarchy based on their eigenvalues. The leading irrelevant eigenoperator of this quadratic Hamiltonian is

$$\mathcal{O}_1 \equiv f_0^\dagger f_1 + H. c., \quad (89)$$

with eigenvalue λ^{-2} , that is,

$$\mathbb{T}[\mathcal{O}_1] = \lambda^{-2} \mathcal{O}_1; \quad (90)$$

therefore, the coefficient $w_1^{\mathcal{N}}$ follows the decay of the energy.

In analogy to c_{res} , the coefficients $w_m^{\mathcal{N}}$ ($m = 1, \dots, \mathcal{M}$) of the irrelevant operators increase in magnitude with λ [35]. Therefore, these operators distinguish $\mathcal{H}_K^{\mathcal{N}}(\lambda)$ from the tight-binding Hamiltonian and push the calculated physical properties away from their continuum values. Consequently, the green curve in Fig. 12 ($\lambda = 3$) shows deviations larger than the orange curve ($\lambda = 2$), and the latter, larger than the blue curve ($\lambda = 1.5$).

To explain the relatively slow time decay of the fluctuations in all three curves, a comparison with equilibrium properties is expedient. Computations of equilibrium properties are focused on a single energy scale: thermodynamical and equilibrium transport properties are associated with the thermal energy scale $k_B T$; spectroscopy, with the photon energy $\hbar\omega$. This energy scale defines the truncation number \mathcal{N} , in analogy with Eq. (78), with the pertinent inverse energy, $1/k_B T$ or $1/\hbar\omega$,

substituted for t/\hbar . The deviation of a physical property caused by the leading operator \mathcal{O}_1 on a given energy scale is then proportional to its coefficient $w_1^{\mathcal{N}}$ and therefore decays with energy. The deviations are therefore insignificant, except at energies that are comparable to the bandwidth.

Time-dependent properties pose a different problem. The uncertainty principle broadens the energy levels by $\Delta_t = \hbar/t$. Instead of an energy scale, this broadening defines a soft cutoff [38]: the energy scales above Δ_t contribute to $\bar{\mathcal{F}}(t)$, although their contribution is a gradually decreasing function of t . At very short times, the sum of all irrelevant operators gives rise to substantial deviations $\Delta\mathcal{F}$. As time increases, the truncation number \mathcal{N} increases, the coefficients of the irrelevant operators decrease, and the operator \mathcal{O}_1 becomes dominant. However, the uncertainty principle admits contributions from higher energy scales, which correspond to smaller truncation numbers \mathcal{N} and hence include other irrelevant operators; as a result, $\Delta\mathcal{F}$ decays more slowly than $1/\omega_\tau t$, as illustrated by the plots in Fig. 12.

V. CONCLUSIONS

We have studied the time dependence of the fidelity $\mathcal{F}(t)$, whose Fourier transform is measured in x-ray photoemission spectroscopy of simple metals. The two general approaches in Secs. III B 1 and III B 2 determine $\mathcal{F}(t)$. The former has led to the analytical expression derived in Appendix A, very accurate for $\omega_\tau t \gg 1$. The latter, which is convenient for numerical computations, has allowed calculation of $\mathcal{F}(t)$ from the eigenvalues and eigenvectors of the tight-binding Hamiltonian for the photoemission problem.

The analytical expression and numerical results of this numerical calculation have served as benchmarks against which we have gauged the precision of the two time-dependent renormalization-group procedures defined in Sec. IV. The results and comparison offer physical and operational insight.

The results highlight the importance of the bound state created by the core-hole potential. As a function of time, the fidelity decays following a power law enveloped by a damped oscillation. The decay is the Doniach-Sunjic power law. The oscillations are due to interference between two kinds of excitation: excitations to plugged states, with the bound state occupied, and to unplugged states, with the bound state vacant. The oscillations are damped because the latter follows the Nozières-De Dominicis power law and, therefore, decays faster than the former, which follows the Doniach-Sunjic law.

We have rooted our developments in the real-space formulation of the renormalization-group

approach, the eNRG method, which generates model Hamiltonians parametrized by two real numbers λ and θ , and an integer ζ . Comparison with benchmarks identified two sources of inaccuracy affecting the fidelities calculated by the eNRG procedures, both due to the discretization of the conduction band. The first source are the irrelevant operators that distinguish the eNRG model Hamiltonians from the fixed points to which the renormalization-group transformation drives them. The irrelevant operators cause slowly decaying transitory deviations. The second source is the reduction of the band continuum to a sequence of discrete levels, which spawns persistent fluctuations and shifts upward the calculated fidelities. ,

The large- ζ procedure, which amounts to working with $\zeta > \omega_\tau t_{\max}$, where t_{\max} is the longest time of interest, produces essentially exact results over the interval $[0, t_{\max}]$. and therefore avoids deviations.

The large- ζ algorithm deals so efficiently with quadratic Hamiltonians and yields so precise fidelities that it has replaced the brute-force procedure and established a more reliable standard of accuracy in our study. We have checked the quality of the fidelities produced by the second eNRG method, the smoothing procedure, against this new benchmark. The second algorithm is valuable because it offers better perspectives for work targeting Hamiltonians with quartic terms. The inability to eliminate transitory deviations limits its range to medium and large times, to wit, the region that may be beyond the scope of the large- ζ method.

In summary, we studied the time dependence of the photoemission current as an object of physical interest in its own right and as a testing ground for the development of time-dependent procedures based on the eNRG method. The analytical expression for the fidelity and the large- ζ algorithm offered (i) solutions to the problem, with results that are uniformly accurate over the one-dimensional parametric space of the model, and (ii) physical interpretation of all features of the solution. With future applications to interacting-impurity Hamiltonians in mind, we have also discussed the smoothing algorithm. Our results show that averaging on ζ followed by integration over θ eliminates persistent deviations and is therefore appropriate to calculate time-dependent properties after the transient deviations have died out.

Acknowledgments - The authors thank Hong-Hao Tu and Jan von Delft for suggesting the single-particle method outlined in Sec. III B 2. This research received financial support from FAPESP (grant 2022/05198-2), the CNPq (grant 311689/2023-0) and the Coordenação de Aperfeiçoamento de Pessoal de Nível Superior – Brasil (CAPES) – Finance Code 001. FDP’s work was supported by PhD and internship fellowships from FAPESP (grants 2022/09312-4 and 2024/05637-1), GD’s by a PhD scholarship from the Brazilian agency Coordenação de Aperfeiçoamento de

Pessoal de Nível Superior (CAPES), and MPL's by an undergraduate research fellowship from FAPESP (2021/11154-5). We gratefully acknowledge the support and access to computational resources offered by the Center for Mathematical Sciences Applied to Industry (CeMEAI), funded by FAPESP (grant 2013/07375-0).

- [1] X. Cui, C. Wang, A. Argondizzo, S. Garrett-Roe, B. Gumhalter, and H. Petek, *Nature Physics* **10**, 505 (2014).
- [2] A. G. Borisov, A. K. Kazansky, and J. P. Gauyacq, *Physical Review B* **59**, 10935 (1999).
- [3] M. Ferrier, T. Arakawa, T. Hata, R. Fujiwara, R. Delagrangé, R. Weil, R. Deblock, R. Sakano, A. Oguri, and K. Kobayashi, *Nature Physics* **12**, 230 (2016).
- [4] F. Cherne III and P. Deymier, *Scripta Materialia* **45**, 985 (2001).
- [5] S. Neppel, R. Ernstorfer, E. M. Bothschafter, A. L. Cavalieri, D. Menzel, J. V. Barth, F. Krausz, R. Kienberger, and P. Feulner, *Physical Review Letter* **109**, 087401 (2012).
- [6] J. M. Donohue, M. Agnew, J. Lavoie, and K. J. Resch, *Phys. Rev. Lett.* **111**, 153602 (2013).
- [7] M. A. Foster, R. Salem, D. F. Geraghty, A. C. Turner-Foster, M. Lipson, and A. L. Gaeta, *Nature* **456**, 81 (2008).
- [8] J. L. Miller, *Physics Today* **71**, 18 (2018), https://pubs.aip.org/physicstoday/article-pdf/71/1/18/10120049/18_1_online.pdf.
- [9] K. H. Rieder, *Contemporary Physics* **26**, 559 (1985).
- [10] T. J. Thornton, *Reports on Progress in Physics* **58**, 311 (1995).
- [11] D. Reguera, J. M. Rubí, and J. M. G. Vilar, *The Journal of Physical Chemistry B* **109**, 21502 (2005).
- [12] T. Fujisawa, T. Hayashi, and S. Sasaki, *Reports on Progress in Physics* **69**, 759 (2006).
- [13] D. M. Kennes, S. G. Jakobs, C. Karrasch, and V. Meden, *Phys. Rev. B* **85**, 085113 (2012).
- [14] M. Zhao, F. Yang, Y. Xue, D. Xiao, and Y. Guo, *ChemPhysChem* **15**, 950 (2014).
- [15] W. Kohn and L. J. Sham, *Physical Review* **140**, A1133 (1965).
- [16] E. Runge and E. K. U. Gross, *Physical Review Letter* **52**, 997 (1984).
- [17] M. A. L. Marques and E. K. U. Gross, *Annual Review of Physical Chemistry* **55**, 427 (2004).
- [18] M. A. L. Marques and E. K. U. Gross, *Advances in Quantum Chemistry* **57**, 1 (2006).
- [19] C. A. Ullrich, *Time-Dependent Density-Functional Theory: Concepts and Applications* (Oxford University Press, 2012).
- [20] S. R. White, *Physical Review Letters* **69**, 2863 (1992).
- [21] S. R. White and A. E. Feiguin, *Physical Review Letters* **93**, 076401 (2004).
- [22] L. G. G. V. Dias da Silva, F. Heidrich-Meisner, A. E. Feiguin, C. A. Büsser, G. B. Martins, E. V. Anda, and E. Dagotto, *Phys. Rev. B* **78**, 195317 (2008).
- [23] S. Trotzky, Y.-A. Chen, A. Flesch, I. P. McCulloch, U. Schollwöck, J. Eisert, and I. Bloch, *Nature*

- Physics **8**, 325 (2012).
- [24] W. Hofstetter and T. Qin, Journal of Physics B: Atomic, Molecular and Optical Physics **51**, 082001 (2018).
 - [25] K. Zawadzki, A. Nocera, and A. E. Feiguin, SciPost Phys. **15**, 166 (2023).
 - [26] N. Schlünzen and M. Bonitz, Contributions to Plasma Physics **56**, 5 (2016).
 - [27] M. Grundner, P. Westhoff, F. B. Kugler, O. Parcollet, and U. Schollwöck, Phys. Rev. B **109**, 155124 (2024).
 - [28] K. G. Wilson, Rev. Mod. Phys. **47**, 773 (1975).
 - [29] D. Goldhaber-Gordon, H. Shtrikman, D. Mahalu, D. Abusch-Magder, U. Meirav, and M. A. Kastner, Nature **391**, 156 (1998).
 - [30] A. K. Mitchell, E. Sela, and D. E. Logan, Phys. Rev. Lett. **108**, 086405 (2012).
 - [31] G. Diniz, G. S. Diniz, G. B. Martins, and E. Vernek, Phys. Rev. B **101**, 125115 (2020).
 - [32] L. O'Brien, M. J. Erickson, D. Spivak, H. Ambaye, R. J. Goyette, V. Lauter, P. A. Crowell, and C. Leighton, Nature Communications **5**, 3927 (2014).
 - [33] I. V. Borzenets, J. Shim, J. C. H. Chen, A. Ludwig, A. D. Wieck, S. Tarucha, H. S. Sim, and M. Yamamoto, Nature **579**, 210 (2020).
 - [34] J.-C. Xu, H. Su, R. Kumar, S.-S. Luo, Z.-Y. Nie, A. Wang, F. Du, R. Li, M. Smidman, and H.-Q. Yuan, Chinese Physics Letters **38**, 087101 (2021).
 - [35] H. R. Krishna-murthy, J. W. Wilkins, and K. G. Wilson, Phys. Rev. B **21**, 1003 (1980).
 - [36] R. Bulla, T. A. Costi, and T. Pruschke, Rev. Mod. Phys. **80**, 395 (2008).
 - [37] R. Bulla, T. Costi, and D. Vollhardt, Physical Review B **64**, 045103 (2001).
 - [38] F. B. Anders and A. Schiller, Phys. Rev. Lett. **95**, 196801 (2005).
 - [39] F. B. Anders and A. Schiller, Phys. Rev. B **74**, 245113 (2006).
 - [40] H. Nghiem and T. Costi, Physical Review B **89**, 075118 (2014).
 - [41] H. Nghiem and T. Costi, Physical Review B **90**, 035129 (2014).
 - [42] F. Schwarz, I. Weymann, J. von Delft, and A. Weichselbaum, Phys. Rev. Lett. **121**, 137702 (2018).
 - [43] M. Lotem, A. Weichselbaum, J. von Delft, and M. Goldstein, Phys. Rev. Res. **2**, 043052 (2020).
 - [44] B. Bruognolo, N.-O. Linden, F. Schwarz, S.-S. B. Lee, K. Stadler, A. Weichselbaum, M. Vojta, F. B. Anders, and J. von Delft, Phys. Rev. B **95**, 121115 (2017).
 - [45] G. D. Mahan, Physical Review **163**, 612 (1967).
 - [46] P. Nozieres and C. T. D. Dominicis, Phys. Rev. **178**, 1097 (1969).
 - [47] S. Doniach and M. Sunjic, J. Phys. C: Solid State Phys. **3**, 285 (1970).
 - [48] M. Combescot and P. Nozières, Journal De Physique **32**, 913 (1971).
 - [49] K. Ohtaka and Y. Tanabe, Reviews of Modern Physics **62**, 929 (1990).
 - [50] A. L. Ferrari and L. N. de Oliveira, Phys. Rev. B **106**, 075129 (2022).
 - [51] W. C. Oliveira and L. N. Oliveira, Physical Review B **49**, 11986 (1994).
 - [52] N. Ashcroft and N. Mermin, *Solid State Physics* (Holt, Rinehart and Winston, New York, 1976).

- [53] T. Fogarty, S. Deffner, T. Busch, and S. Campbell, Physical Review Letters **124**, 110601 (2020).
- [54] P. W. Anderson, Phys. Rev. Lett. **18**, 1049 (1967).
- [55] H. R. Krishna-murthy, J. W. Wilkins, and K. G. Wilson, Phys. Rev. B **21**, 1044 (1980).

Appendix A: Derivation of Eq. (56)

The derivation of the analytical expression (56) for the *fidelity*, $\mathcal{F}(t)$, involves a number of approximations, which become reliable under the conditions $\omega_\tau t \gg 1$ and $L \gg 1$. The first approximation amounts to replacing the tight-binding dispersion relation (22) by the linear form (23), which we rewrite here in the equivalent form

$$\varepsilon_q = \Delta_L \left(q + \frac{1}{2} \right) \quad (q = -L, -(L-1), \dots, L-1), \quad (\text{A1})$$

with $\Delta_L \equiv \tau\pi/L$. This approximation loses accuracy near the borders of the conduction band, that is, for $q \approx \pm L$, a shortcoming that affects the precision of Eq. (56) at short times only.

For consistency, we also adopt an expression equivalent to the linearized Eqs. (25), which represent the single-particle eigenvalues of the final Hamiltonian:

$$\epsilon_\ell = \Delta_L \left(\ell + \frac{1}{2} - \frac{\delta}{\pi} \right) \quad (\ell = -(L-1), -(L-2), \dots, L-1), \quad (\text{A2})$$

and

$$\epsilon_{-L} = \begin{cases} \Delta_L \left(-L + \frac{1}{2} - \frac{\delta}{\pi} \right) & (|K| < \tau) \\ -(K + \frac{\tau^2}{K}) & (|K| \geq \tau). \end{cases} \quad (\text{A3})$$

In addition, we take let the phase shift δ be the constant given by Eq. (26), although that equality is only exact at the Fermi level.

Under these assumptions, the commutator between an initial eigenstate a_q^\dagger and a final one b_ℓ is given by Eq. (29), to wit,

$$\{a_q^\dagger, b_\ell\} = \frac{\sin(\delta)}{\pi} \frac{1}{q - \ell + \frac{\delta}{\pi}}, \quad (\text{A4})$$

for all q and ℓ , except $\ell = -L$.

As explained in Sec. III B 4, the many-body eigenstates of the final Hamiltonian can be divided into two disjoint classes of plugged $|r_P\rangle$ and unplugged $|r_U\rangle$ states. In this notation, Eq. (18) reads

$$\mathcal{F}(t) = \left| \sum_{r_P} |\langle r_P | \Omega_0 \rangle|^2 \exp\left(-i \frac{E_{r_P}}{\hbar} t\right) + \sum_{r_U} |\langle r_U | \Omega_0 \rangle|^2 \exp\left(-i \frac{E_{r_U}}{\hbar} t\right) \right|^2 \quad (\text{A5})$$

where $|\Omega_0\rangle$ is the many-body ground state of the initial Hamiltonian ($K = 0$).

1. Plugged eigenstates

In the many-body ground state of the initial Hamiltonian, all single-particle levels $\epsilon_n < 0$, below the Fermi level ($n = -1, -2, \dots, -L$), are occupied, while the other levels remain vacant. Therefore,

$$|\Omega_0\rangle = \prod_{j=-L}^{-1} a_j^\dagger |\emptyset\rangle. \quad (\text{A6})$$

where $|\emptyset\rangle$ is the vacuum state.

Likewise, in the many-body ground state $|\Omega\rangle$ of the final Hamiltonian, all single-particle levels ϵ_n below the Fermi level ($n = -1, -2, \dots, -L$) are occupied:

$$|\Omega\rangle = \prod_{j=-L}^{-1} b_j^\dagger |\emptyset\rangle. \quad (\text{A7})$$

By definition, $|\Omega\rangle$ is a plugged state. Other plugged states consist of particle-hole excitations from the ground state that leave the bound level occupied. The number k of particle-hole excitations ranges from $k = 1$ to $k = L - 1$.

With this in mind, we can associate each plugged state $|r_P\rangle$ containing k particle-hole excitations ($k = 1, \dots, L - 1$) with two unique sets of k integers:

$$\{p\} \equiv \{p_1, p_2, \dots, p_k\} \quad (0 \leq p_1 < p_2 < \dots < p_k \leq L - 1), \quad (\text{A8})$$

and

$$\{h\} \equiv \{h_1, h_2, \dots, h_k\} \quad (-1 \geq h_1 > h_2 > \dots > h_k > -L), \quad (\text{A9})$$

so that the energy levels indexed by the p_j ($j = 1, \dots, k$) lie above the Fermi level and are filled, while the levels indexed by h_j lie below and are vacant.

The condition $h_k > -L$ ensures that the bound level is filled. The labels in Eq. (A8) and (A9) are ordered so that p_1 and h_1 are closest in energy. When these two labels are excluded, p_2 and h_2 are closest in energy, and so forth until p_k and h_k . Alternatively, the two equations establish a sequence of electron-hole pairings in increasing energy order.

Given the sets $\{p\}$ and $\{h\}$, the eigenstate $|r_P\rangle$ can be written as

$$|r_P\rangle = \prod_{j=1}^k b_{p_j}^\dagger b_{h_j} |\Omega\rangle, \quad (\text{A10})$$

and its energy measured from the ground state as

$$E_{r_P} = \Delta_L \sum_{j=1}^k (p_j - h_j). \quad (\text{A11})$$

where we used Eq. (A2).

It will be helpful to define a third set $\{g\}$. To this end, let $\{g_0\} \equiv \{-1, -2, \dots, -L\}$ and define $\{g\}$ as the complement of $\{h\}$ with respect to $\{g_0\}$. In other words, whereas $\{h\}$ contains the k labels of the negative energy levels that are vacant in $|r_P\rangle$, the set $\{g\}$ contains the labels of the $L - k$ negative energy levels that remain occupied. Like the levels in $\{h\}$, the elements of $\{g\}$ are arranged in descending energy order. Since $|r_P\rangle$ is a plugged state, $g_{L-k} = -L$.

From Eq. (A10), it follows that the projection of $|r_P\rangle$ onto the initial ground state is

$$\langle r_P | \Omega_0 \rangle = \langle \Omega | \prod_{j=1}^k b_{h_j}^\dagger b_{p_j} | \Omega_0 \rangle. \quad (\text{A12})$$

It is instructive to first consider the special case $k = 0$, that is, the projection $\langle \Omega | \Omega_0 \rangle$. Wick's theorem guarantees that this projection is a sum of $L!$ products, each of which is a contraction between L final-state operators b_ℓ ($\ell = -L, \dots, -1$) from $\langle \Omega |$ and L initial-state operators a_q^\dagger ($q = -L, \dots, -1$) from $| \Omega_0 \rangle$. The contractions are given by the anticommutators in Eq. (A4). This case highlights the importance of the contribution from *diagonal contractions*, that is, contractions between operators with the same index $q = \ell$, which yield the anticommutators with the largest absolute value:

$$\{b_q, a_q^\dagger\} = \frac{\sin(\delta)}{\delta} \quad (q = -L, \dots, -1); \quad (\text{A13})$$

in particular, for $\delta \rightarrow 0$, the right-hand side of Eq. (A13) becomes unitary, while the right-hand side of Eq. (A4) vanishes for all off-diagonal ($q \neq \ell$) anticommutators.

This contrasts with the projections of excited states, with $k > 0$. The single-particle states b_{p_j} ($j = 1, \dots, k$) now have positive energies and cannot pair with the initial states. Whereas the Wick expansion of $\langle \Omega | \Omega_0 \rangle$ contains a term with L diagonal contractions, the corresponding term in the expansion of $\langle r_P | \Omega_0 \rangle$ contains only $L - k$ diagonal contractions. Thus, the absolute value $|\langle r_P | \Omega_0 \rangle|$ is smaller than $|\langle \Omega | \Omega_0 \rangle|$. In other words, excited states with large k contribute relatively little to the fidelity. For this reason, our analysis focuses on final many-body states with small numbers k , of particle-hole excitations.

For $k > 0$, we can define the partial many-body projection

$$\langle \Omega | \Omega_0 \rangle_k \equiv \langle \emptyset | \prod_{j=1}^{L-k} b_{g_j} a_{g_j}^\dagger | \emptyset \rangle, \quad (\text{A14})$$

which involves the occupied negative-energy levels in $|r_P\rangle$ and the initial-state levels with the same labels.

In addition to these levels, the right-hand side of Eq. (A12) involves the positive energy final eigenstates b_{p_j} and the negative energy initial eigenstate a_{h_j} ($j = 1, 2, \dots, k$). As Eq. (A4) shows the anticommutators between initial eigenstate operators and a final ones increase in magnitude when the energy difference between them decreases. It is therefore a good approximation to contract each b_{p_j} with the a_{h_j} that is closest in energy, that is, in the pairing order defined by Eqs. (A8) and (A9). Explicitly, this approximation reads

$$\langle r_P | \Omega_0 \rangle = \langle \Omega | \Omega_0 \rangle_k \prod_{j=1}^k \left\{ b_{p_j}, a_{h_j}^\dagger \right\}. \quad (\text{A15})$$

With the same accuracy, the projection of $|\Omega\rangle$ upon $|\Omega_0\rangle$ can be written as

$$\langle \Omega | \Omega_0 \rangle = \langle \Omega | \Omega_0 \rangle_k \prod_{j=1}^k \left\{ b_{h_j}, a_{h_j}^\dagger \right\}. \quad (\text{A16})$$

Substitution of Eq. (A4) on the right-hand sides of Eqs. (A15) and (A16) yields the following equalities:

$$\langle r_P | \Omega_0 \rangle = \langle \Omega | \Omega_0 \rangle_k \prod_{j=1}^k \left(\frac{\sin(\delta)}{\pi} \frac{1}{h_j - p_j + \frac{\delta}{\pi}} \right), \quad (\text{A17})$$

and

$$\langle \Omega | \Omega_0 \rangle = \langle \Omega | \Omega_0 \rangle_k \left(\frac{\sin(\delta)}{\delta} \right)^k. \quad (\text{A18})$$

Division of Eq. (A17) by Eq. (A18) now eliminates the common factor $\langle \Omega | \Omega_0 \rangle_k$,

$$\langle r_P | \Omega_0 \rangle = \langle \Omega | \Omega_0 \rangle \left(\frac{\delta}{\pi} \right)^k \prod_{j=1}^k \frac{1}{h_j - p_j + \frac{\delta}{\pi}}. \quad (\text{A19})$$

We can now substitute the right-hand sides of Eq. (A19) for $\langle r_P | \Omega_0 \rangle$ and Eq. (A11) for E_{r_P} in the first term on the right-hand side of Eq. (A5), to determine the contribution (47) of the plugged states to the fidelity:

$$\mathcal{P}_P(t) = \langle \Omega | \Omega_0 \rangle^2 \sum_{r_P} \left(\frac{\delta}{\pi} \right)^{2k} \prod_{j=1}^k \frac{\exp(-i(p_j - h_j)\omega_L t)}{\left(h_j - p_j + \frac{\delta}{\pi} \right)^2}, \quad (\text{A20})$$

where

$$\omega_L \equiv \frac{\Delta_L}{\hbar} = \frac{2\pi}{T_L}. \quad (\text{A21})$$

Each many-body eigenstate $|r_P\rangle$ is characterized by a number k of particle-hole excitations and the sets $\{p\}$ and $\{k\}$ in Eqs. (A8) and (A9), respectively. Therefore, summing over $|r_P\rangle$ amounts to summing over k and, for each k , summing over all distributions of p_j and h_j consistent with Eqs. (A8) and (A9), respectively.

The set $\{p\}$ can be regarded as a vector \mathbf{p} in a k -dimensional vector space \mathcal{V}_P , with components p_1, p_2, \dots, p_k . The inequalities on the right-hand side of Eq. (A8) restrict \mathbf{p} to a subsector of \mathcal{V}_P . The boundaries of the subspace are also excluded by the strict inequalities; however, this restriction is inconsequential, as the number of points in the boundaries is $\mathcal{O}(1/L)$, relative to the number of points in \mathcal{V}_P .

The labeling of any pair p_i, p_j of elements in $\{p\}$ can be freely interchanged, provided that the labeling of the corresponding pair h_i, h_j in $\{h\}$ also be interchanged. Therefore, we can enumerate all permutations of the elements in $\{p\}$ to form a class of $k!$ vectors that span the entire space \mathcal{V}_P . This allows us to eliminate the inequalities so that Eqs. (A8) and (A9) become

$$\{p\} \equiv \{p_1, p_2, \dots, p_k\} \quad (1 \leq p_j \leq L; j = 1, \dots, L), \quad (\text{A22})$$

and

$$\{h\} \equiv \{h_1, h_2, \dots, h_k\} \quad (-L < h_j \leq -1; j = 1, \dots, L), \quad (\text{A23})$$

respectively.

These simplifications bring Eq. (A20) to the form

$$\mathcal{P}_P(t) = \langle \Omega | \Omega_0 \rangle^2 \sum_{k=0}^L \frac{1}{k!} \left(\frac{\delta}{\pi} \right)^{2k} \prod_{j=1}^k \sum_{p_j=0}^{L-1} \sum_{h_j=-(L-1)}^{-1} \frac{\exp(-i(p_j - h_j)\omega_L t)}{\left(h_j - p_j + \frac{\delta}{\pi} \right)^2}. \quad (\text{A24})$$

For large L , the Euler-Maclaurin summation formula converts the two sums on the right-hand side of Eq. (A24) into integrals. This approximation yields the expression

$$\mathcal{P}_P(t) = \langle \Omega | \Omega_0 \rangle^2 \sum_{k=0}^L \frac{1}{k!} \left(\frac{\delta}{\pi} \right)^{2k} \prod_{j=1}^k \int_0^{L-1} \int_{-L+1}^{-1} \frac{\exp(-i(p-h)\omega_L t)}{\left(h - p + \frac{\delta}{\pi} \right)^2} dh dp, \quad (\text{A25})$$

or with the substitution $q \equiv h - p + \delta/\pi$ for the inner integration variable,

$$\mathcal{P}_P(t) = \langle \Omega | \Omega_0 \rangle^2 \sum_{k=0}^L \frac{1}{k!} \left(\frac{\delta}{\pi} \right)^{2k} \prod_{j=1}^k e^{i\omega_L \frac{\delta}{\pi} t} \int_0^{L-1} \int_{-L+1-p+\frac{\delta}{\pi}}^{-1-p+\frac{\delta}{\pi}} \frac{e^{iq\omega_L t}}{q^2} dq dp. \quad (\text{A26})$$

To compute the integral over q on the right-hand side of Eq. (A26), it is expedient define the function

$$\Phi(q) \equiv -\frac{e^{iq\omega_L t}}{q}, \quad (\text{A27})$$

and differentiate it with respect to q :

$$\frac{d\Phi}{dq} = \frac{e^{iq\omega_L t}}{q^2} - i\omega_L t \frac{e^{iq\omega_L t}}{q}. \quad (\text{A28})$$

From Eq. (A21), we have that $t \ll T_L$ implies $\omega_L t \ll 1$, which justifies the withdrawal of the second on the term on the right-hand side of Eq. (A28). This approximation turns $\Phi(q)$ into a primitive of the integrand on the right-hand side of Eq. (A26). The inequality $\omega_L t \ll 1$ also makes the exponential multiplying the integrals on the right-hand side approximately unitary and leads to

$$\mathcal{P}_P(t) = \langle \Omega | \Omega_0 \rangle^2 \sum_{k=0}^L \frac{1}{k!} \left(\frac{\delta}{\pi} \right)^{2k} \prod_{j=1}^k \int_0^{L-1} \left(\Phi \left(-1 - p + \frac{\delta}{\pi} \right) - \Phi \left(-L + 1 - p + \frac{\delta}{\pi} \right) \right) dp. \quad (\text{A29})$$

Equation (A27) shows that the second term within parentheses in the integrand on the right-hand side of Eq. (A29) vanishes as $L \rightarrow \infty$ and can be ignored. Making $r = p + 1 - \delta/\pi$ the integration variable, we have that

$$\mathcal{P}_P(t) = \langle \Omega | \Omega_0 \rangle^2 \sum_{k=0}^L \frac{1}{k!} \left(\frac{\delta}{\pi} \right)^{2k} \left(\int_{1-\frac{\delta}{\pi}}^{L-\frac{\delta}{\pi}} \frac{e^{-ir\omega_L t}}{r} dr \right)^k. \quad (\text{A30})$$

Since the summand on the right-hand side of Eq. (A30) decays rapidly with k , it is safe to extend the upper limit to infinity and convert the sum into an exponential, which reduces the equality to the form

$$\mathcal{P}_P(t) = \langle \Omega | \Omega_0 \rangle^2 \exp \left(\left(\frac{\delta}{\pi} \right)^2 \int_{1-\frac{\delta}{\pi}}^{L-\frac{\delta}{\pi}} \frac{e^{-ir\omega_L t}}{r} dr \right). \quad (\text{A31})$$

At $t = 0$, since $L \gg \delta/\pi$, the integral on the right-hand side equals $\ln(L - \delta/\pi) - \ln(1 - \delta/\pi) \approx \ln(L)$. Recalling that $L\omega_L z t = \pi\omega_\tau t$, with the change of variables $x = \omega_\tau t$ and other straightforward manipulations, we can rewrite Eq. (A31) in the equivalent form

$$\mathcal{P}_P(t) = \mathcal{P}_P(0) \exp \left(- \left(\frac{\delta}{\pi} \right)^2 \int_0^{\pi\omega_\tau t} \frac{1 - \cos(x)}{x} dx \right) \exp \left(-i \left(\frac{\delta}{\pi} \right)^2 \int_0^{\pi\omega_\tau t} \frac{\sin(x)}{x} dx \right), \quad (\text{A32})$$

or, with the shorthand (57), which defines \mathcal{T}_t as the exponential of the first integral on the right-hand side,

$$\mathcal{P}_P(t) = \mathcal{P}_P(0) \mathcal{T}_t^{-\left(\frac{\delta}{\pi}\right)^2} \exp \left(-i \left(\frac{\delta}{\pi} \right)^2 \int_0^{\pi\omega_\tau t} \frac{\sin(x)}{x} dx \right). \quad (\text{A33})$$

2. Unplugged eigenstates

The ground state of the final Hamiltonian is a plugged state by definition. The lowest energy unplugged state $|\Omega_U\rangle$ is the one in which only the lowest L single particle energy levels above the bound state are occupied,

$$|\Omega_U\rangle = b_1^\dagger b_{-1}^\dagger \dots b_{-L+1}^\dagger |\emptyset\rangle. \quad (\text{A34})$$

As explained in Sec. III B 4, the energy difference between $|\Omega_U\rangle$ and $|\Omega\rangle$ is ϵ_B , that is, the difference between the first positive single-particle energy and the bound-state energy. The other unplugged states can be constructed by considering k ($k = 1, 2, \dots, L-1$) particle-hole excitations above $|\Omega_U\rangle$, care being taken to keep the bound level vacant. Like $|r_P\rangle$, a generic unplugged state $|r_U\rangle$ with k particle-hole excitations is described by two sets of labels: $\{p\} = \{1 < p_1 < p_2 < \dots < p_k \leq L\}$ and $\{h\} = \{-L < h_1 < h_2 < \dots < h_k \leq 1\}$, in analogy with Eqs. (A8) and (A9), respectively. The unplugged state is then given by the equality

$$|r_U\rangle = \prod_{j=1}^k b_{p_j}^\dagger b_{h_j} |\Omega_U\rangle, \quad (\text{A35})$$

its energy, measured from the ground state, is

$$E_{r_U} = \epsilon_B + \Delta_L \sum_{j=1}^k (p_j - h_j), \quad (\text{A36})$$

and its projection over the initial ground state is

$$\langle r_U | \Omega_0 \rangle = \langle \Omega_U | \prod_{j=1}^k b_{h_j}^\dagger b_{p_j} | \Omega_0 \rangle. \quad (\text{A37})$$

For $k = 0$, the right-hand side of Eq. (A37) reduces to the overlap $\langle \Omega_U | \Omega_0 \rangle$, given by Wick's Theorem, as before. However, now the initial single-particle eigenvectors cannot be contracted with the bound level, which is vacant. Thus, the lowest diagonal contraction pairs a_{-L}^\dagger with b_{-L+1} ; a_{-L+1}^\dagger with b_{-L} ; and so on until a_{-1}^\dagger with b_1 . The corresponding anticommutators, given by Eq. (A4), are

$$\{b_{q+1}, a_q^\dagger\} = \frac{\sin(\delta)}{\delta - \pi} \quad (q = -L, \dots, -1). \quad (\text{A38})$$

Equation (A36), (A37) and (A38) are analogous to Eqs. (A11), (A12) and (A13), respectively. Keeping in mind the distinction between the former trio and the latter, we can start at Eq. (A37)

and follow the algebraic sequence from Eq. (A12) to (A33) to derive the following expression for the contribution (48) of the unplugged states to the fidelity:

$$\mathcal{P}_U(t) = \mathcal{P}_U(0) \mathcal{T}_t^{-\left(1 - \frac{\delta}{\pi}\right)^2} \exp\left(-i \left(1 - \frac{\delta}{\pi}\right)^2 \int_0^{\pi\omega_\tau t} \frac{\sin(x)}{x} dx\right). \quad (\text{A39})$$

where

$$\mathcal{P}_U(0) = \left\langle \Omega_U \middle| \Omega_0 \right\rangle^2 L \left(1 - \frac{\delta}{\pi}\right)^2. \quad (\text{A40})$$

3. Fidelity

To exploit the similarity between Eqs. (A32) and (A43) for $\mathcal{P}_P(t)$ and $\mathcal{P}_U(t)$, it is useful to define the ratio

$$Q \equiv \frac{\mathcal{P}_U(0)}{\mathcal{P}_P(0)}, \quad (\text{A41})$$

and the function

$$\vartheta_t = \left(1 - \frac{2\delta}{\pi}\right) \text{Si}(\pi\omega_\tau t), \quad (\text{A42})$$

so that Eq. (A39) can be written as

$$\mathcal{P}_U(t) = Q \mathcal{T}_t^{-\left(1 - \frac{2\delta}{\pi}\right)} \exp(-i\vartheta_t) \mathcal{P}_P(t). \quad (\text{A43})$$

We can then substitute the right-hand sides of Eqs. (A32) and (A43) in Eq. (45) to obtain the fidelity

$$\mathcal{F}(t) = \left|1 + \mathcal{R}_t \exp(-i(\omega_B t + \vartheta(t)))\right|^2 \mathcal{T}_t^{-2\left(\frac{\delta}{\pi}\right)^2} |\mathcal{P}_P(0)|^2, \quad (\text{A44})$$

where \mathcal{R}_t , defined by Eq. (58), is the ratio between $Q \mathcal{T}_t^{-\beta}$ and $\mathcal{T}_t^{-\alpha}$.

From the definitions of $\mathcal{F}(t)$, \mathcal{T}_t , \mathcal{R}_t , and ϑ_t we have that $\mathcal{F}(0) = \mathcal{T}_{t=0} = 1$, $\mathcal{R}_{t=0} = Q$, and $\vartheta_{t=0} = 0$. With these initial values, Eq. (A44) implies that

$$|\mathcal{P}_P(0)|^2 = \frac{1}{(1 + Q)^2}, \quad (\text{A45})$$

and substitution of the right-hand side for the last factor in Eq. (A44) yields Eq. (56).